A Thesis for the Degree of Master of Engineering

Analysis of Tsunami Resonance in Coastal Waters

Advisor JoongWoo Lee

August, 2012

Graduated School of Korea Maritime University

Department of Civil and Environmental Engineering

Kyu Kwang Kim

本 論文을 金 奎 光의 工學碩士 學位論文으로 認准함.

委員長 工學博士 鞠 承 淇 (印)

委 員 工學博士 金 泰 亨 (印)

委 員 工學博士 李 重 雨 (印)

2012年 8月

韓國海洋大學校 大學院

土 木 環 境 工 學 科

金 奎 光

Contents

Analysis of Tsunami Resonance in Coastal Waters

Kyu-Kwang Kim

Department of Civil and Environmental Engineering
Graduate School of Korea Maritime University

ABSTRACT

Recently, extreme tsunami waves generated by submarine earthquake have caused tremendous damages to the coastal cities and ports. Strong seiche oscillations and runups are observed in specific sea areas around the world. When multiple destructive tsunamis caused damage to Japan, Chile, USA, Indonesia, New Zealand, they have been recognized as a potential hazard to Korean coastal communities. Although no frequent impacts to the coast of Korean peninsula, there were some important events in the east of Korea in the past.

This study focuses on two historical events and recalculate with different fault and rupture mechanism for prediction considering the recent trend of submarine earthquake. Three-dimensional, time dependent, nonlinear, incompressible, viscous flow calculations were performed of realistic models of tsunami waves interacting with continental slopes and shelves.

The present study of the 1983 Akita tsunamis demonstrates the multi-scale resonance along continental coasts. Together with the Nankai

tsunami for inland sea, we have confirmed the inland sea resonance surrounded by islands in defining the impact along the coast. The damping action of submerged barriers on tsunami waves was investigated. Significant amounts of the energy of a tsunami were reflected by submerged barriers or coastal boundaries. Coherence and wavelet analyses for deducing a predominant period and time frequency are useful in reasoning the inundation.

   The resonance modes, which are largely independent of the tsunami source, allow identification of at-risk communities and infrastructure for mitigation of tsunami hazards. The numerical simulation of tsunami waves can provide realistic descriptions of their propagation. Furthermore, understanding of the resonance and the predicted runups for the site of power plant and industrial complex in the east coast of Korea would allow better preparation for the future disasters.

LIST OF TABLES

LIST OF FIGURES

Chapter 1 Introduction

1.1 Background and Objectives

The scale of destruction and unprecedented loss of life following the December 2004 Sumatra tsunami involved as the catalyst to refocus international efforts on reducing tsunami vulnerability of coastal communities. However, the 2011 Tohoku-Pacific Ocean earthquake over Mw 9.0 had generated the most destructive mega tsunami in history in the east coast of Japan and across the Pacific Ocean. Most of coastal countries are worrying about not just for the tsunami runup disasters but also exposure to radioactive contamination. Each country had started to investigate the safeness of the site and facilities and to discuss the disaster prevention media. Even the scientists and researchers, who are the expert on the tsunami prediction, are busy to investigate again the earthquake parameters and static and dynamic generation mechanism for tsunamis that had occurred already. They check all possibilities of change in terms of subfault, strike angle, slip, rupture duration, earthquake scale, and manning coefficients, etc.

The Korean peninsula is subject to tsunamis only generated from the East Sea, source of submarine earthquake near the west coast of Japan: Hokkaido and northern part of Honshu. Fig.1.1 shows the submarine eqrthquakes along the Korean coast after 2000 and the tsunami events which had hit the Korean coast are shown in Fig.1.2 (Kim et al, 2011).

Most of tsunamis generated by the earthquakes of Pacific Ocean rim are protected by Japan and are not reached to Korean Peninsula, except this

sea. Although the history of impact of tsunamis are minor for the east coast of Korea, there were two significant impacts from tsunamis in 1983 and 1993 from the submarine earthquakes at the west coast of Japan and caused damages along the Korean coast, not just for port facilities but flooding due to runups along the low land coastline. On May 26, 1983, an earthquake with 7.7 Mw occurred at 40.4N and 139.1E in the west coast of Japan. The resulting tsunami reached the entire west coast of Japan and east coast of Russia and Korea. This had caused serious damage to near coast of Japan, Aomori, Akita and the southwestern part of Hokkaido, together with the mid-eastern coast of South Korea, Imwon. Some harbors and embayment had experienced prolonged oscillations with amplitudes. Fig.1.3 shows the study area for the large basin(blue line) and narrow inland sea area(red line).

There are 32 nuclear power plants sites in South Korea including 24 reactors in operation now. Most of nuclear power plants are located in the east coast, except Yonggwang plant as shown in Fig.1.4 and Table 1.1.
The reactors of nuclear power plants are classified into 4 types such as Pressurized Water Reactor (PWR, Light), Pressurized Heavy Water Reactor (PHWR), Korean Standardized Nuclear Plant (KSNP), Optimized Power Reactor (OPR-1000), and Advanced Pressurized Reactor (APR-1400). Besides these, there are some important industrial complex in the east coast such as POSCO Pohang steel company, Ulsan Oil refinery, Hyundai ship building and motor company, and new ports. Therefore, it is believed that investigation and recalculation on the design level for these facilities with respect to tsunami event are very important and necessary procedure. For that purpose in the first step, we tried to investigate tsunami wave resonance in these coastal boundaries.
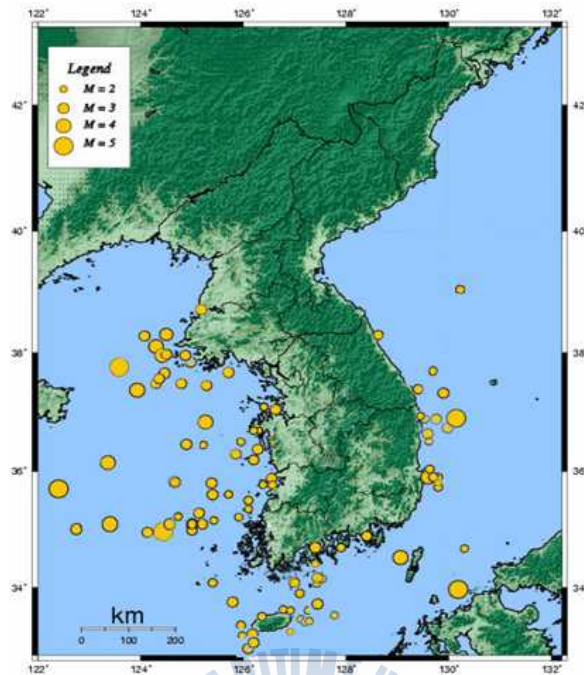
Fig.1.1 Submarine earthquake record since 2000 (after Kim et al, 2011)
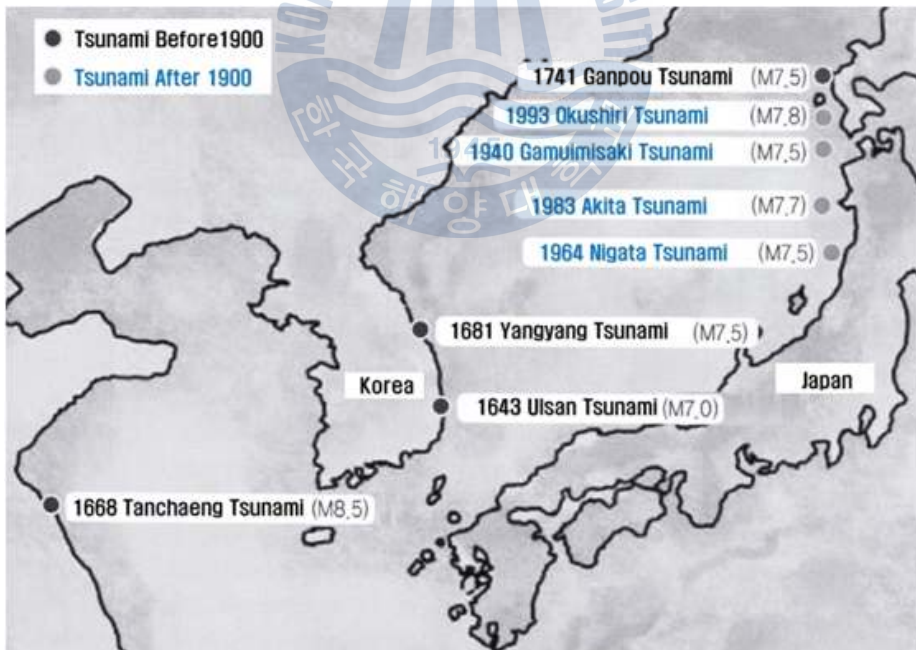
Fig.1.2 Historical record of tsunami generation in Korea
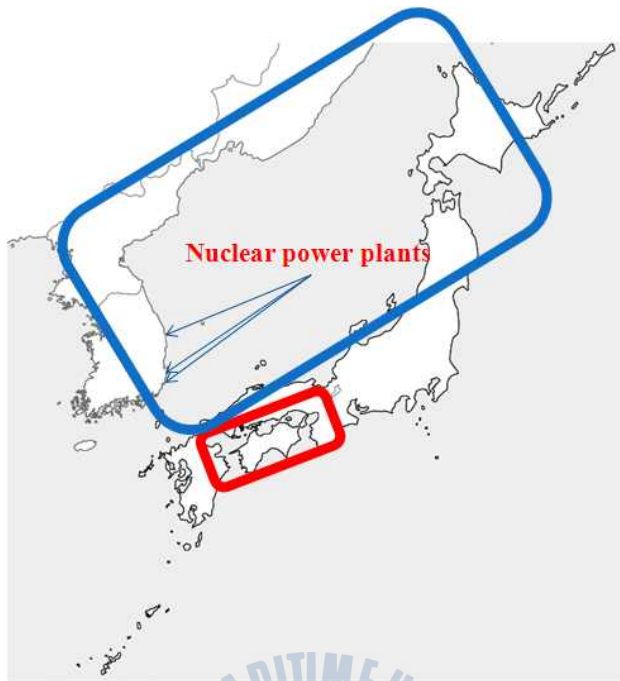
Fig.1.3 Study area for tsunami response

Fig.1.4 Location map for the nuclear power plants in South Korea (●)

Table 1.1 Specification of current and planned nuclear power capacity in the Republic of Korea (MKE, 2010)

Site	Unit	Type	Capacity (MWe)	Initial Operation
Kori	Kori-1	PWR(Westing- house)USA	587	Apr.1978
	Kori-2	PWR(Westing- house)USA	650	Jul.1983
	Kori-3	PWR(Westing- house)USA	950	Sept.1985
	Kori-4	PWR(Westing- house)USA	950	Apr.1986
	Sinkori-1	PWR(OPR-1000)	1000	Dec.2010
	Sinkori-2	PWR(OPR-1000)	1000	Dec.2011(test)
	Sinkori-3	PWR(OPR-1400)	1400	Sept.2013(test)
	Sinkori-4	PWR(OPR-1400)	1400	Sept.2014
	Sinkori-5	PWR(OPR-1400)	1400	Dec.2018
	Sinkori-6	PWR(OPR-1400)	1400	Dec.2019
Yonggwang	Yonggwang-1	PWR(Westinghouse)USA	950	Aug. 1986
	Yonggwang-2	PWR(Westinghouse)USA	950	Jun. 1987
	Yonggwang-3	PWR(System 80)	1000	Mar. 1995
	Yonggwang-4	PWR(System 80)	1000	Jan. 1996
	Yonggwang-5	PWR(KSNP)	1000	Apr. 2002
	Yonggwang-6	PWR(KSNP)	1000	Oct. 2002
Ulchin	Ulchin-1	PWR(Framatone)France	950	Sept. 1988
	Ulchin-2	PWR(Framatone)France	950	Sept. 1989
	Ulchin-3	PWR(KSNP)	1000	Aug. 1988
	Ulchin-4	PWR(KSNP)	1000	Dec. 1999
	Ulchin-5	PWR(KSNP)	1000	Jul. 2004
	Ulchin-6	PWR(KSNP)	1000	Jun. 2005
	Sinulchin-1	PWR(APR-1400)	1400	Jun.2016
	Sinulchin-2	PWR(APR-1400)	1400	Jun.2017
	Sinulchin-3	PWR(APR-1400)	1400	Dec. 2020
	Sinulchin-4	PWR(APR-1400)	1400	Dec. 2021
Wolsong	Wolsong-1	PHWR(CANDU) Canada	679	Apr. 1983
	Wolsong-2	PHWR(CANDU) Canada	700	Jul. 1997
	Wolsong-3	PHWR(CANDU) Canada	700	Jul. 1998
	Wolsong-4	PHWR(CANDU) Canada	700	Oct. 1999
Wolsong	Sinwolsong-1	PWR(OPR-1000)	1000	Oct.2011(test)
	Sinwolsong-1	PWR(OPR-1000)	1000	Oct.2011(test)

On the other hand, tsunami impact to the inland waters causes notice to the coastal water and inland water users such as aqua-farmers, and fishery and shipping industries. Investigation on tsunami wave resonance in a bay or inland sea is also necessary for the purpose of analyzing the impact on

navigation and reason mooring facilities. One important location for inland sea is noticed to the Seto inland sea, as shown in Fig.1.3. It is located at the western part of Japan and surrounded by Honshu, Kyushu and Shikoku Islands. The coastal area of Shikoku Island has been frequently ravaged by huge Nankai earthquake tsunamis which had occurred along the Nankai trough. Resonance phenomena were noticed in the Seto inland sea, especially Harima-Nada area. Investigation on oscillation at inland sea due to tsunami input is also necessary for disaster prevention purpose.

Fig.1.5 Location map of large inland sea area in Japan

The tsunami forecasting capability, based on models and measurements, including tsunami inundation models and hazard maps, is a central component for the protection coastlines of Korea and Japan from the threat posed by tsunamis.

1.2 Major Tsunami Disasters in Korea-Japan Sea

1) Nihonkai-Chubu Tsunami(1983)

The Nihonkai-Chubu tsunami generated by a magnitude 7.9 (Mw) earthquake destroyed 700 boats and 59 houses for a total of $800 million in property damage in Japan (1983 dollars). One hundred and four people drowned in Japan and three drowned in Korea. At least 104 people killed, some injured, and extensive damage to dwellings, roads, and vessels caused by earthquake and a tsunami along the Japan Sea coast from southern Hokkaido to the Niigata area, Honshu. Many of the casualties and much of the damage occurred on the Oga Peninsula. Tsunami damage occurred as far away as Yamaguchi Prefecture in southwestern Honshu, along the Japan Sea coast of USSR, and along the eastern and southern coasts of South Korea, where three additional people were killed. Estimated tsunami heights were 14 meters at Minehama, Honshu, 2-6 meters along southern Hokkaido and northern Honshu, up to 8 meters along the coast of USSR, and 4 meters along the coast of South Korea.
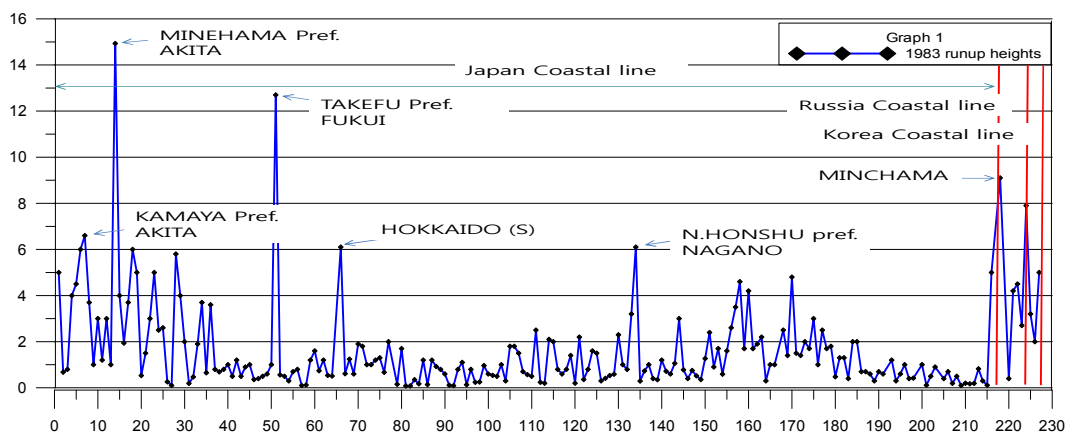
Fig.1.6 Elevated runup heights in 1983 Tsunami

2) Okushiri-Hokaido Tsunami(1993)

The Hokkaido Nansei-oki earthquake of M7.8 occurred in 1993. The earthquake generated tsunami which caused devastating damages especially in Okushiri Island, Hokkaido Prefecture. The number of victims due to both tsunami and earthquake was 230 in Japan. Approximately 80% of the victims in Okushiri Island were due to the tsunami: 172 dead and 26 missing. The tsunami climbed a steep hill surface up to 31.7m at the Monai area in Okushiri Island, being affected by the bathymetric and topographic conditions. Part of the Aonae area on a southern headland of Okushiri Island was attacked by the tsunami with runup height of over 10m.

Consequently all of the 77 houses located in the low lying flat area were absolutely destroyed. Another reason for the large number of casualties was the fact that the tsunami arrived at Okushiri Isalnd just 3-5 minutes after the eqrthquake because the epicenter was located approximately 50km off Okushiri Island.

Damage of nearly half a million dollars occurred, mostly to fishing boats and equipment. Damage was caused to a factory at Kamenka, Sakhalin Island, and to Vladivostok, Russia, which reported two-meter waves. Waves with heights up to four meters were observed on the Primorye coasts of Russia. Damage in Russia exceeded $6.5 million.
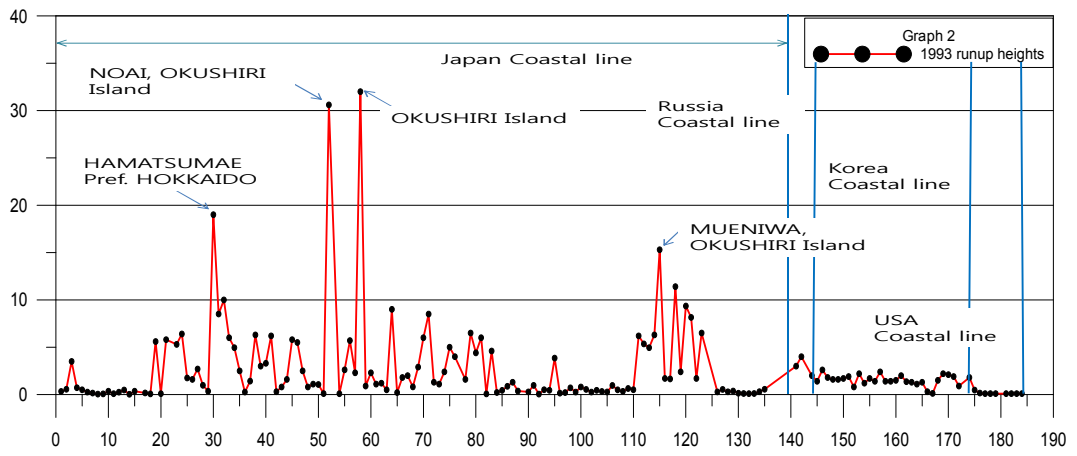
Fig.1.7 Elevated runup heights in 1993 Tsunami

Chapter 2 Tsunami Characteristics

2.1 Basic Description

Tsunami is a series of ocean waves generated by sea surface displacement which is mainly produced by earthquake, volcanic eruption, and massive sediment inflow induced by landslide. Development of the tsunami wave can be distinguished by : 1) the transmission of the disturbance to the water mass, 2) the propagation of the surface gravity wave over a great distance across the deep ocean, and 3) the transformation of the wave near the shore. The basic description of tsunami with an incompressible, homogeneous, and non-viscous ocean is subjected to a constant gravitational field with a rigid seafloor. Linear theory assumes that the ratio of wave amplitude to wavelength is much less than one. Although linear wave theory may not fit in every situation, the assumption of linearity presents easier superposition and spectrally decomposition of waveforms. In classical theory, the phase velocity $c(\sigma)$, and group velocity $c_g(\sigma)$ of surface gravity waves on uniform water depth h are

$$c(\sigma) = \sqrt{\frac{gh\tanh\left[k(\sigma)h\right]}{k(\sigma)h}} \qquad (2.1)$$

$$c_g(\sigma) = c(\sigma)\left[\frac{1}{2} + \sqrt{\frac{k(\sigma)h}{\sinh\left[2k(\sigma)h\right]}}\right] \qquad (2.2)$$

Here, g is the acceleration of gravity ($9.81 m/s^2$) and $k(\sigma)$ is the wave number associated with a wave angular frequency σ. Wave length is related to wave number $\lambda(\sigma) = 2\pi k(\sigma)$ and wave number also satisfies

the exact dispersion relation $\sigma^2 = kg(\sigma)\tanh[k(\sigma)h]$. The linear dispersion relation from the classical Boussinesq equations of Peregrine (1967) is given by $c(\sigma)^2 = gh/(1+[k(\sigma)h]^2/3)$ and the depth-integrated, non-hydrostatic equation by Yamazaki (2010) is $c(\sigma)^2 = gh/(1+[k(\sigma)h]^2/4)$. Fig.2.1 compares the linear dispersion relations and it provides the depth-integrated, non-hydrostatic equation is well fit for the exact solution.
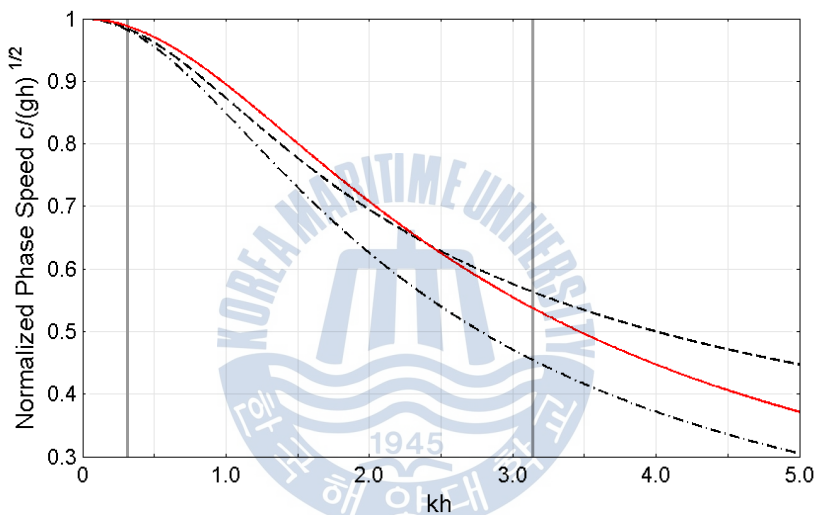
Fig. 2.1 Comparison of linear dispersion relation (after Yamazaki, 2010)
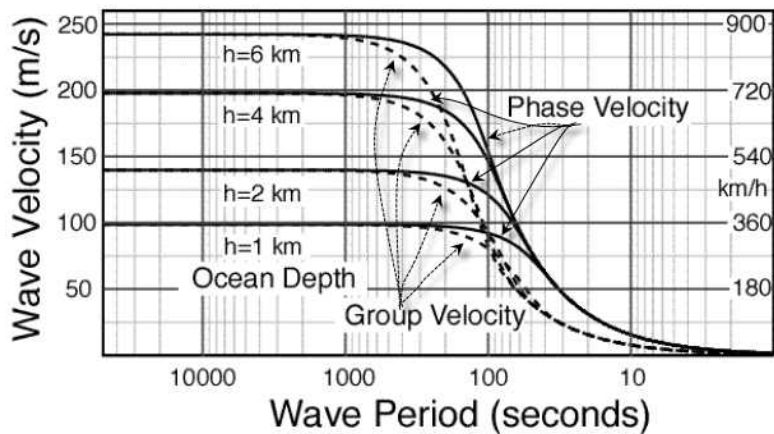
Fig. 2.2 Wave velocities on a flat water depth (after Wald,2000)

From the linear wave theory, tsunami waves through surface gravity wave propagation and transformation show these quantities in terms of water depth and wave period as shown in Fig.2.2.

2.2 Excitation of Tsunami

When the seafloor uplift instantaneously by earthquake or submarine volcano activity, it generates tsunami waves. The deformation creates a similar displacement on the sea surface right above the sea floor. For the case of the seafloor at points r_0 uplift time $\tau(r_0)$ by amount of vertical motion of seafloor $u_z^{bot}(r_0)$, in a uniform ocean of depth h, this bottom disturbance triggers surface tsunami waveforms $u_z^{surf}(r,t)$ at observation point $r = xi + yj$ and the corresponding rupture initiation time t of (Ward, 2000)

$$u_z^{surf}(r,t) = Re \int_k dk \, \frac{e^{j[k \cdot r - \sigma(k)t]}}{4\pi^2 \cosh(kh)} F_i(k) \tag{2.4}$$

$$F_i(k) = \int_{r_0} dr_0 \, u_z^{bot}(r_0, \tau(r_0)) e^{-i[k \cdot r_0 - \sigma(k)\tau(r_0)]} \tag{2.5}$$

where $dk = dk_x dk_y$, $dr_0 = dx_0 dy_0$, and the integrals cover all wave number space and locations r_0 where the seafloor disturbance $u_z^{bot}(r_0) \neq 0$. The equation $F_i(k)$ is the wave number spectrum of the seafloor uplift, which relates to the amplitude, spatial, and temporal distribution of the uplift.

The planar fault model of Okada (1985) describes the ground surface deformation in terms of the depth, orientation, and slip of a rectangular fault as shown in Fig.2.3. The deformation is a linear function of the slip

and dimensions of the fault. Superposition of the planar fault solutions from the subfaults gives the time sequence of the vertical displacement of the seafloor as

$$\eta(\boldsymbol{r},t) = \sum_{i=1}^{n} \eta_i(\boldsymbol{r}) f_i(t) \qquad (2.6)$$

where

$$f_i(t) = \begin{cases} 0 & if \quad t < t_i \\ \dfrac{t - t_i}{\tau_i} & if \quad t_i \leq t \leq (t_i + \tau_i) \\ 1 \end{cases} \qquad (2.7)$$

in which η_i is the vertical ground surface deformation associated with rupture of subfault i from Okada (1985).
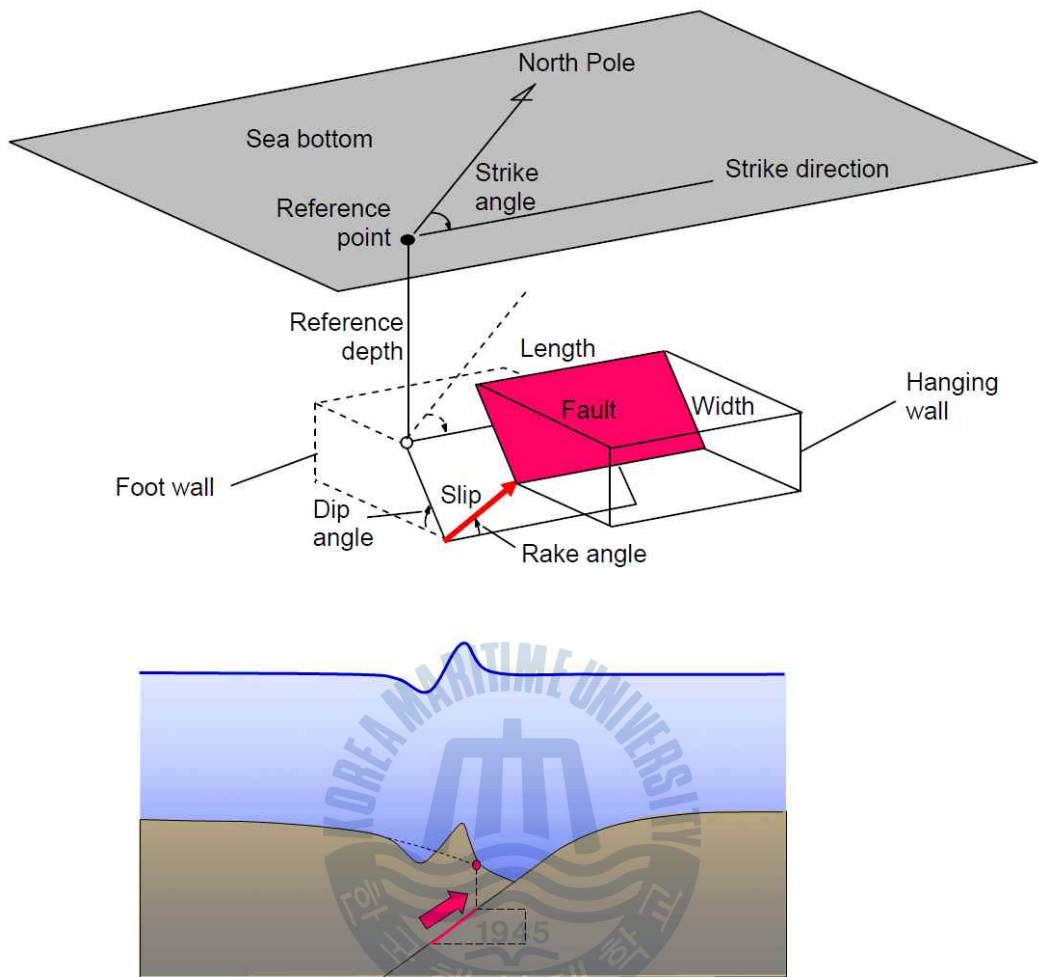
Fig. 2.3 Fault parameters and sea floor deformation

Chapter 3 Numerical Simulation

3. 1 Governing Equations

In computation of far field tsunamis which travel over the ocean, the dispersion term becomes important as the long travel distance acts to disperse wave components. Yamazaki (2010) describes the governing equations for three-dimensional momentum and the continuity equations in the spherical coordinates (λ, ϕ, D) with a radius R of the earth, in which λ is the longitude and is the latitude, and D is the flow depth that the distance normal to the two boundaries $D = \zeta + (h - \eta)$, where ζ is the surface elevation from the still water level, h is the water depth, and η is the seafloor displacement. Fig.3.1 provides a schematic of the free surface flow generated by seafloor deformation.
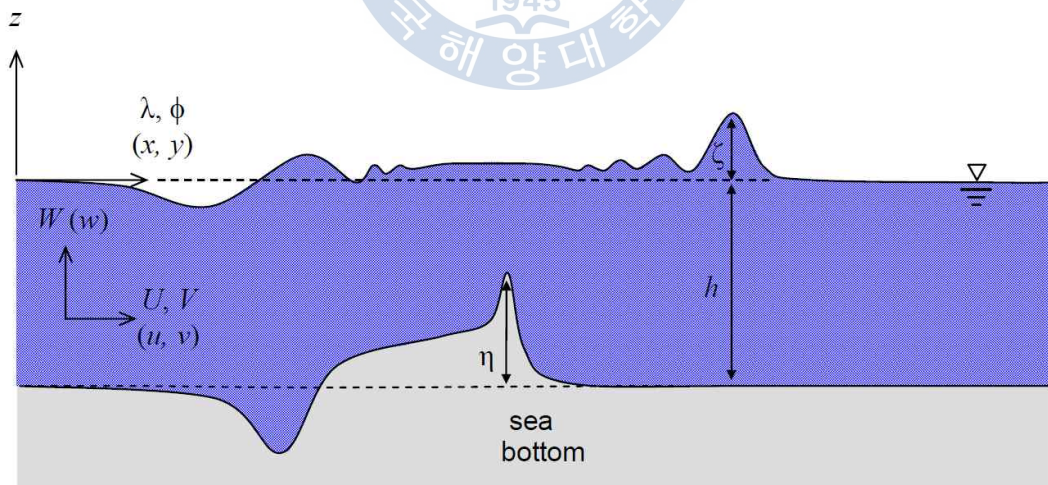
Fig.3.1 Schematic of the free surface flow generated by seafloor deformation

The depth integrated, non-hydrostatic governing equations are in the form

$$\frac{\partial U}{\partial t} + \frac{U}{Rcos\phi}\frac{\partial U}{\partial \lambda} + \frac{V}{R}\frac{\partial U}{\partial \phi}\left(2\Omega + \frac{U}{Rcos\phi}\right)Vsin\phi =$$
$$-\frac{g}{Rcos\phi}\frac{\partial \zeta}{\partial \lambda} - \frac{1}{2}\frac{1}{Rcos\phi}\frac{\partial q}{\partial \lambda} - \frac{1}{2}\frac{q}{DRcos\phi}\frac{\partial(\zeta - h + \eta)}{\partial \lambda} - f\frac{U\sqrt{U^2 + V^2}}{D} \tag{3.1}$$

$$\frac{\partial V}{\partial t} + \frac{U}{Rcos\phi}\frac{\partial V}{\partial \lambda} + \frac{V}{R}\frac{\partial V}{\partial \phi} + \left(2\Omega + \frac{U}{Rcos\phi}\right)Usin\phi =$$
$$-\frac{g}{R}\frac{\partial \zeta}{\partial \lambda} - \frac{1}{2}\frac{1}{R}\frac{\partial q}{\partial \phi} - \frac{1}{2}\frac{q}{DR}\frac{\partial(\zeta - h + \eta)}{\partial \phi} - f\frac{V\sqrt{U^2 + V^2}}{D} \tag{3.2}$$

$$\frac{\partial W}{\partial t} = \frac{q}{D} \tag{3.3}$$

$$\frac{\partial(\zeta - \eta)}{\partial t} + \frac{1}{Rcos\phi}\frac{\partial(UD)}{\partial \lambda} + \frac{1}{Rcos\phi}\frac{\partial(Vcos\phi D)}{\partial \phi} = 0 \tag{3.4}$$

where U, V, W are the dept have raged velocity components; t is time; Ω is the earth's angular velocity; g is the gravitation acceleration; q is the non-hydrostatic pressure; and f is a dimensionless friction factor given in terms of Manning's relative roughness coefficient n as $f \backsimeq n^2 g / D^{1/3}$.

For near field tsunamis, the Cartesian coordinate system is used because the areas included in model simulations are not wide, where effect of the earth's curvature is insignificant. Therefore, the governing equations in the spherical coordinate system can be transformed into the Cartesian coordinates system and the momentum and continuity equations are transformed into equations (3.5) through (3.7).

$$\frac{\partial U}{\partial t} + U\frac{\partial U}{\partial x} + V\frac{\partial U}{\partial y} = -g\frac{\partial \zeta}{\partial x} - \frac{1}{2}\frac{\partial q}{\partial x} - \frac{1}{2}\frac{q}{D}\frac{\partial}{\partial x}(\zeta - h + \eta) - f\frac{U\sqrt{U^2 + V^2}}{D} \qquad (3.5)$$

$$\frac{\partial V}{\partial t} + U\frac{\partial V}{\partial x} + V\frac{\partial V}{\partial y} = -g\frac{\partial \zeta}{\partial y} - \frac{1}{2}\frac{\partial q}{\partial y} - \frac{1}{2}\frac{q}{D}\frac{\partial}{\partial y}(\zeta - h + \eta) - f\frac{V\sqrt{U^2 + V^2}}{D} \qquad (3.6)$$

$$\frac{\partial(\zeta - \eta)}{\partial t} + \frac{\partial(UD)}{\partial x} + \frac{\partial(VD)}{\partial y} = 0 \qquad (3.7)$$

The finite difference formulation utilizing the upwind flux approximation in the continuity equation as well as the advective terms in the horizontal momentum equations is adopted for the hydrostatic and non-hydrostatic components of the governing equations in both the spherical and Cartesian coordinate systems. Grid-nesting scheme for the model by Yamazaki et al. (2006) was adopted here. Model uses the Cartesian coordinate grids with the fluxes, the velocity, surface elevation as well as the non-hydrostatic pressure as input variables to a fine inner grid and the surface elevation as output to the outer grid.

3.2 Spherical Coordinate System Model

The numerical formulation includes the solution scheme for the governing equations in spherical grid system. Upwind flux finite difference approximation of Mader (1988) was introduced in the calculation of the continuity equation and the advective terms in the horizontal momentum equation. Fig.3.2 shows the space-staggered grid for the computation. For inundation or runup calculations, wet-dry moving boundary condition (by Kowalik and Murty, 1993) was adopted.
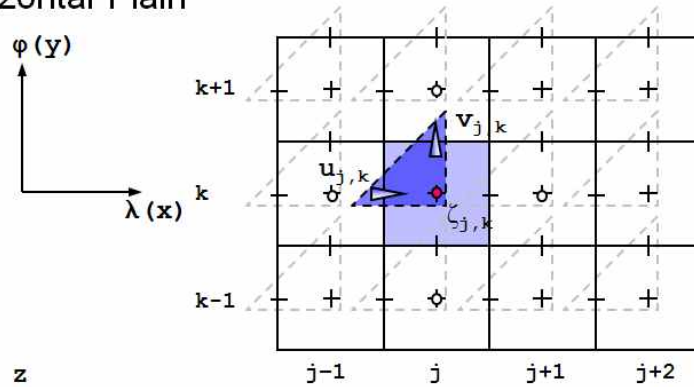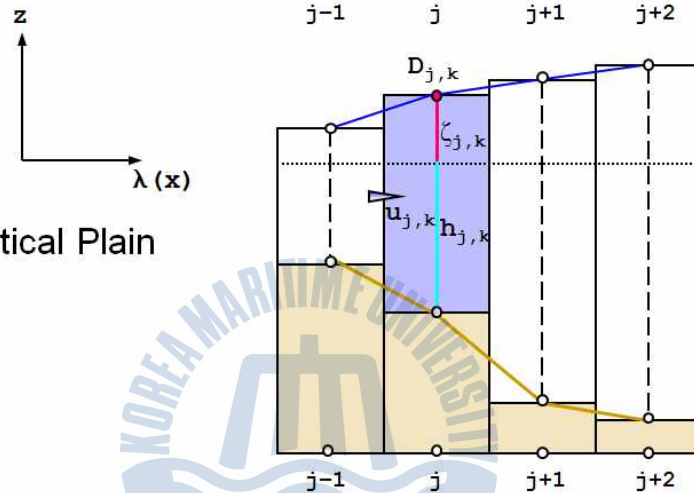
Fig. 3.2 Definition sketch of spatial grid.

Integration of the non-hydrostatic terms in the horizontal momentum equations completes the update of the horizontal velocity from (3.1) and (3.2).

$$U_{j,k}^{m+1} = \widetilde{U}_{j,k}^{m+1} - \frac{\Delta t}{R\Delta\lambda\cos\phi_k} A_{j,k} \frac{(q_{j,k}^{m+1} + q_{j-1,k}^{m+1})}{2}$$
$$- \frac{\Delta t}{R\Delta\lambda\cos\phi_k} \frac{(q_{j,k}^{m+1} - q_{j-1,k}^{m+1})}{2} \tag{3.8}$$

$$V_{j,k}^{m+1} = \widetilde{V}_{j,k}^{m+1} - \frac{\Delta t}{R\Delta\lambda\cos\phi_k} A_{j,k} \frac{(q_{j,k}^{m+1} + q_{j-1,k}^{m+1})}{2}$$
$$- \frac{\Delta t}{R\Delta\lambda\cos\phi_k} \frac{(q_{j,k}^{m+1} - q_{j-1,k}^{m+1})}{2} \tag{3.9}$$

where

$$\widetilde{U}_{j,k}^{m+1} = U_{j,k}^m - \frac{g\Delta t}{R\Delta\lambda\cos\phi_k}(\zeta_{j,k}^m - \zeta_{j-1,k}^m) + \Delta t\left(2\Omega + \frac{U_{j,k}^m}{R\cos\phi_k}\right)\overline{V}_{x,j,k}^m\sin\phi_k$$

$$- \frac{\Delta t}{R\Delta\lambda\cos\phi_k} U_p^m(U_{j,k}^m - U_{j-1,k}^m) - \frac{\Delta t}{R\Delta\lambda\cos\phi_k} U_n^m(U_{j+1,k}^m - U_{j,k}^m)$$

$$- \frac{\Delta t}{R\Delta\phi} \overline{V}_{x,p}^m(U_{j,k}^m - U_{j,k-1}^m) - \frac{\Delta t}{R\Delta\phi} \overline{V}_{x,n}^m(U_{j,k+1}^m - U_{j,k}^m)$$

$$- n^2g\frac{\Delta t\, U_{j,k}^m \sqrt{(U_{j,k}^m)^2 + (\overline{V}_{x,j,k}^m)^2}}{(D_{j-1,k}^m + D_{j,k}^m)^{\frac{4}{3}}} \tag{3.10}$$

$$\widetilde{V}_{j,k}^{m+1} = V_{j,k}^m - \frac{g\Delta t}{R\Delta\phi}(\zeta_{j,k+1}^m - \zeta_{j,k}^m)$$

$$- \Delta t\left(2\Omega + \frac{\overline{U}_{y,j,k}^m}{R\cos(\phi_k + \Delta\phi/2)}\right)\overline{U}_{y,j,k}^m\sin(\phi_k + \Delta\phi/2)$$

$$- \frac{\Delta t}{R\Delta\lambda\cos(\phi_k + \Delta\phi/2)} \overline{U}_{yp}^m(V_{j,k}^m - V_{j-1,k}^m)$$

$$- \frac{\Delta t}{R\Delta\lambda\cos(\phi_k + \Delta\phi/2)} \overline{U}_{yn}^m(V_{j+1,k}^m - V_{j,k}^m)$$

$$- \frac{\Delta t}{R\Delta\phi} V_p^m(V_{j,k}^m - V_{j,k-1}^m) - \frac{\Delta t}{R\Delta\phi} V_n^m(V_{j,k+1}^m - V_{j,k}^m)$$

$$- n^2g\frac{\Delta V_{j,k}^m \sqrt{(\overline{U}_{y,j,k}^m)^2 + (V_{j,k}^m)^2}}{(D_{j,k}^m + D_{j,k+1}^m)^{\frac{4}{3}}} \tag{3.11}$$

where the subscripts p and n indicates upwind and downwind approximations of the advective speeds , and $\overline{U}$ and $\overline{V}$ are average velocity components are defined by

$$\overline{U_{y,j,k}^m} = \frac{1}{4}\left(U_{j,k}^m + U_{j+1,k}^m + U_{j+1,k+1}^m + U_{j,k+1}^m\right) \tag{3.12}$$

$$\overline{V_{x,j,k}^m} = \frac{1}{4}\left(V_{j,k}^m + U_{j-1,k}^m + U_{j-1,k-1}^m + U_{j,k-1}^m\right) \tag{3.13}$$

$$A_{j,k} = \frac{\left(\zeta_{j,k}^m - h_{j,k} + \eta_{j,k}^m\right) - \left(\zeta_{j-1,k}^m - h_{j-1,k} + \eta_{j-1,k}^m\right)}{\left(D_{j,k}^m + D_{j-1,k}^m\right)} \tag{3.14}$$

$$B_{j,k} = \frac{\left(\zeta_{j,k+1}^m - h_{j,k+1} + \eta_{j,k+1}^m\right) - \left(\zeta_{j,k}^m - h_{j,k} + \eta_{j,k}^m\right)}{\left(D_{j,k}^m + D_{j,k+1}^m\right)} \tag{3.15}$$

Discretization of the vertical momentum equation (3.3) gives the vertical velocity at the free surface as

$$w_{s,j,k}^{m+1} = w_{s,j,k}^m - (w_{b,j,k}^{m+1} - w_{b,j,k}^m) + \frac{2\Delta t}{D_{j,k}^m}q_{j,k}^{m+1} \tag{3.16}$$

where the vertical velocity at the seafloor w_b is evaluated from the boundary condition at $z = -h + \eta$ as

$$w = \frac{\partial \eta}{\partial t} - \frac{U}{Rcos\phi}\frac{\partial(h-\eta)}{\partial \lambda} - \frac{V}{R}\frac{\partial(h-\eta)}{\partial \phi} \tag{3.17}$$

Integration of the continuity equation (3.4) provides an update of the surface elevation at the center of cell (j,k) in terms of the fluxes, FLX and FLY, along the longitude and latitude at the cell interfaces as;

$$\zeta_{j,k}^{m+1} = \zeta_{j,k}^m + (\eta_{j,k}^{m+1} - \eta_{j,k}^m) - \Delta t \frac{FLX_{j+1,k} - FLX_{j,k}}{R\Delta\lambda\cos\phi_k} \tag{3.18}$$

$$- \Delta t \frac{FLY_{j,k}\cos(\phi_k + \Delta\phi/2) - FLY_{j,k-1}\cos(\phi_{k-1} + \Delta\phi/2)}{R\Delta\phi\cos\phi_k}$$

where m denotes the time step, Δt the time step size, and $\Delta\lambda$ and $\Delta\phi$ the respective grid sizes. The upwind flux approximation (3.18) extrapolates the surface elevation from the upwind cell, while the water depth takes on the average value from the two adjacent cells (Mader, 1988). Titov and Synolakis (1988) proposed the flux with a second order scheme as;

$$FLX_{j,k} = U_{j,k}^{m+1} \frac{(\zeta_{j-1,k}^m + h_{j-1,k} - \eta_{j-1,k}^m) + (\zeta_{j,k}^m + h_{j,k} - \eta_{j,k}^m)}{2} \tag{3.19}$$

$$FLY_{j,k} = U_{j,k}^{m+1} \frac{(\zeta_{j,k}^m + h_{j,k} - \eta_{j,k}^m) + (\zeta_{j,k+1}^m + h_{j,k+1} - \eta_{j,k+1}^m)}{2} \tag{3.20}$$

Substitution of (3.8), (3.9) and (3.13) into the continuity equation (3.14) gives a linear system of Poisson-type equations at all grid cells in the form of

$$[P](q) = \{Q\} \tag{3.21}$$

Where $[P]$ is a poisson type non-symmetric metrix and $\{Q\}$ is the load vector of the forcing term. This equation defines the physics of the non-hydrostatic processes, which describe the seafloor, free-surface, and velocity gradients in the generation and modification of dispersive waves.

The non-hydrostatics solution of the surface elevation is calculated by equation (3.18). Details of the parameters are well described in NEOWAVE by Cheung & Yamazaki (2010).

Spherical coordinate system model was applied to the case for 1983 Akita earthquake event, subfault 1 and 2 (Aida, 1984) as shown in Table 3.1, because of wide area for tsunami propagation. The numerical model reproduces the amplitude of the tsunami time series and the frequency contents in the spectrum. Fig.3.3 shows the location and bathymetry for the nested grid. In the center of East sea (Japan sea), there exists Daewhatoe (Yamato Rise) and it causes wave concentration to this area and scattering behind it. Fig.3.5 shows the sea surface configuration right after the rupture.

The main energy for the resulting tsunami propagated toward the west coast of Japan and Russia and Korean coasts. Fig.3.6 indicates the tsunami wave amplitude over the East sea (Japan sea) with a maximum value of 1.5m over the deep ocean. The tsunami propagates away from the rupture in radial directions. The Daewhatoe refracts and traps the radiated energy initially as progressive edge waves on the shelf of Korean coast. The trapped waves at the coast of North Korea oscillate at the natural periods of the embayment and emit long period waves into the open ocean for several hours. Fig.3.7 is the computed wave forms and spectra at Ewashi and Iwanai of Houshu, Japan.

The model produces the initial positive wave and captures the distinct 60 and 100-min oscillations. The energy bands cover the natural periods of oscillation of large scale coastal bathymetric features resulting in the amplification across the Korean coast. Fig.3.8 shows sum of the maximum water level at the east coast of Korea for 7 hours of tsunami propagation period. Youngil-Bay in south Korea and Younghung and Hamhung Bay in

north Korea show the strong responses. Especially Imwon, near the center of the coast had strong response. The arrows indicate the location of nuclear power plants. Red color indicates strong response more than 2.5m runup. More than 2m of water level was shown in the mid of Korean coast.

Table 3.1 Subfault parameters (after Aida, 1984)

Fault No.	Lat(°N)	Long(°E)	d(km)	θ(°)	δ(°)	λ(°)	L(km)	W(km)	Slip(m)
①	40.21	138.84	2	22	40	90	40	30	7.6
②	40.54	139.02	3	355	25	80	60	30	3.05
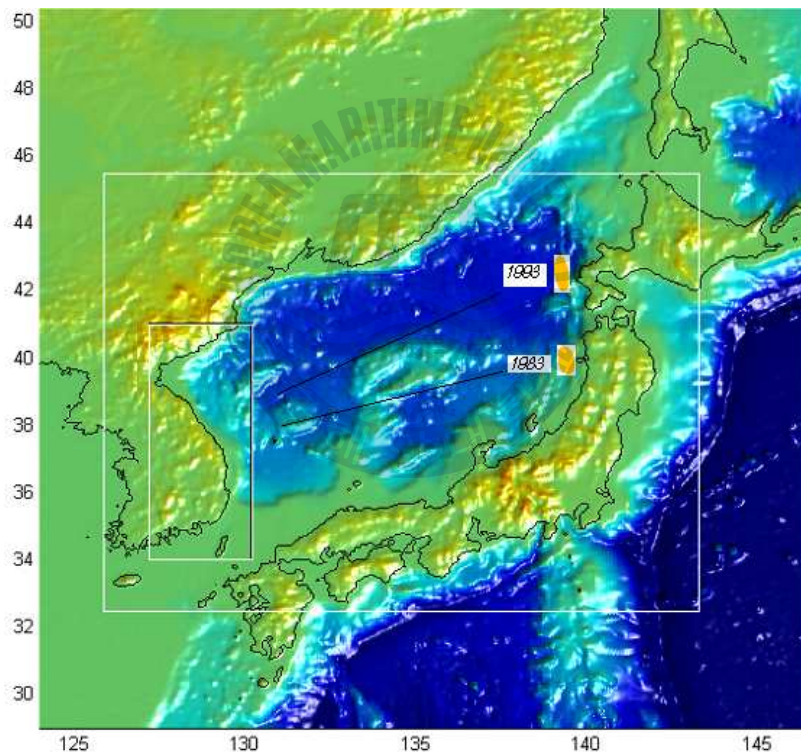
Fig.3.3 Location map and topography for Nested grid 1 and grid 2

- 23 -
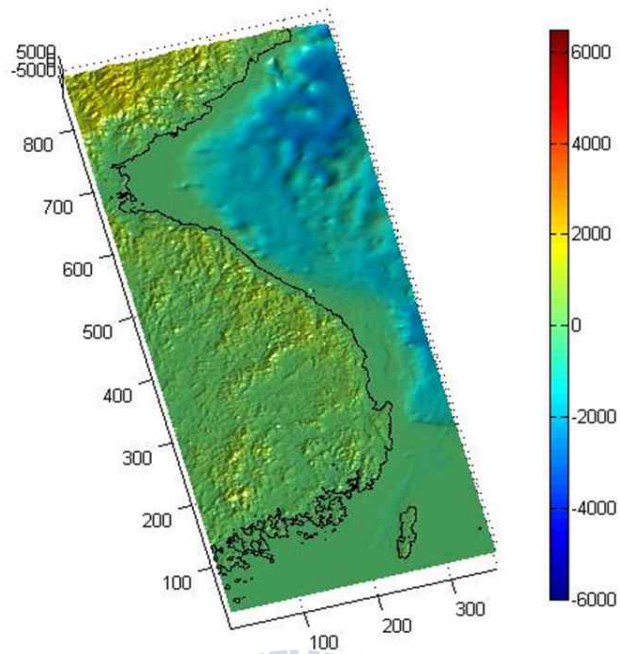
Fig.3.4 Location map and topography for Nested grid 2
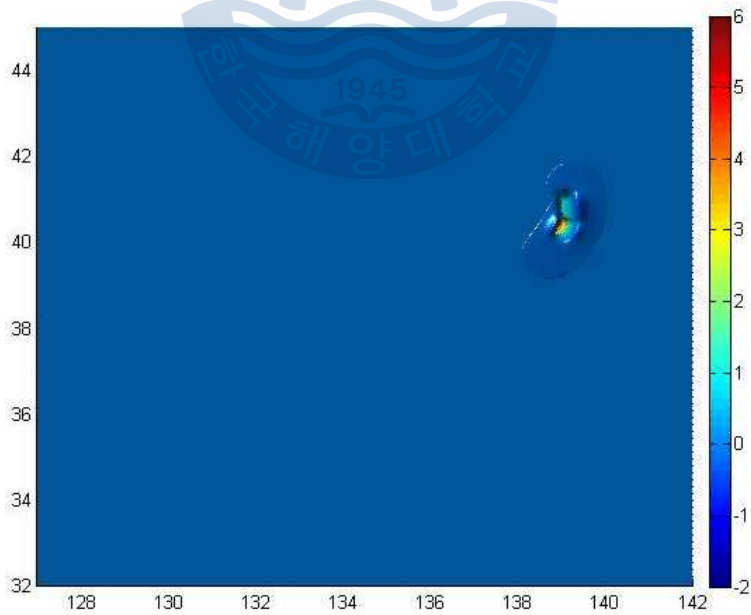
Fig.3.5 Initial response of Akita earthquake in 1983
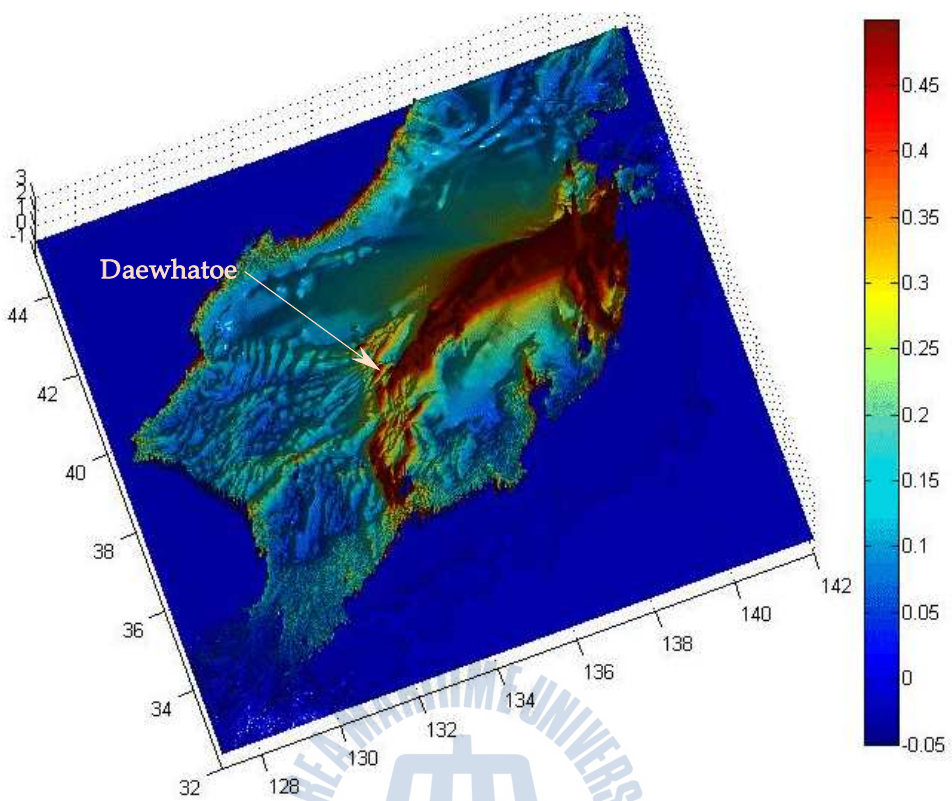
Fig.3.6 Maximum responses for 1983 tsunami
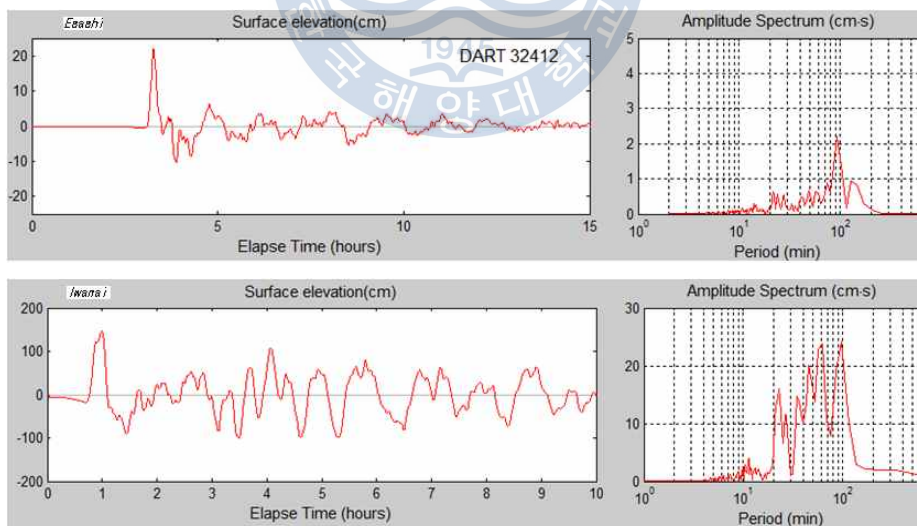
Fig.3.7 Time series and spectra of surface elevation at water-level stations at Ewashi and Iwanai areas
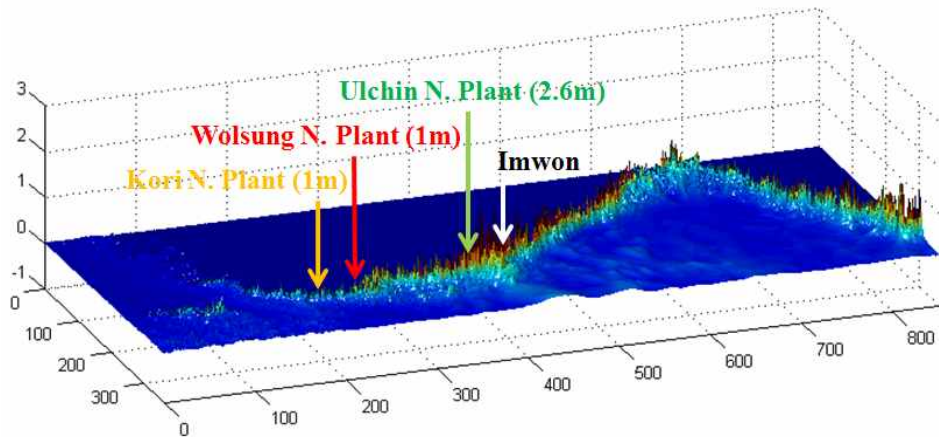
Fig.3.8 Maximum water level at the east coast of Korea

3.3 Cartesian Coordinate System Model

The numerical formulation in the Cartesian coordinate system can be obtained from the discretized form of the coordinate transformation in (3.5) through (3.7).

The integration of the hydrostatic terms in the momentum equations gives

$$
\widetilde{U}_{j,k}^{m+1} = U_{j,k}^m - \frac{g\Delta t}{\Delta x}(\zeta_{j,k}^m - \zeta_{j-1,k}^m) - \frac{\Delta t}{\Delta x} U_p^m\left(U_{j,k}^m - U_{j-1,k}^m\right)
$$
$$
- \frac{\Delta t}{\Delta x} U_n^m\left(U_{j+1,k}^m - U_{j,k}^m\right) - \frac{\Delta t}{\Delta y} \overline{V}_{x,p}^m\left(U_{j,k}^m - U_{j,k-1}^m\right)
$$

$$
- \frac{\Delta t}{\Delta y} \overline{V}_{x,n}^m\left(U_{j+1,k}^m - U_{j,k}^m\right) - n^2 g \frac{\Delta t U_{j,k}^m \sqrt{\left(U_{j,k}^m\right)^2 + \left(\overline{V}_{x,j,k}^m\right)^2}}{\left(D_{j-1,k}^m + D_{j,k}^m\right)^{\frac{4}{3}}}
\tag{3.22}
$$

$$\widetilde{V}_{j,k}^{m+1} = V_{j,k}^m - \frac{g\Delta t}{\Delta y}(\zeta_{j,k+1}^m - \zeta_{j,k}^m) - \frac{\Delta t}{\Delta x}\overline{U}yp^m(V_{j,k}^m - V_{j,k}^m)$$

$$- \frac{\Delta t}{\Delta x}Vp^m(V_{j,k}^m - V_{j,k-1}^m) - \frac{\Delta t}{\Delta y}Vn^m(V_{j,k+1}^m - V_{j,k}^m)$$

$$- n^2 g \frac{\Delta t\, V_{j,k}^m \sqrt{\left(\overline{U}_{y,j,k}^m\right)^2 + \left(V_{j,k}^m\right)^2}}{\left(D_{j,k}^m + D_{j,k+1}^m\right)^{\frac{4}{3}}} \tag{3.23}$$

The explicit time integration of the depth-integrated continuity equation becomes

$$\zeta_{j,k}^{m+1} = \zeta_{j,k}^m - \Delta t\frac{\left(FLX_{j+1,k} - FLX_{j,k}\right)}{\Delta x} - \Delta t\frac{\left(FLY_{j,k} - FLY_{j,k-1}\right)}{\Delta y} \tag{3.24}$$

Substitution of (3.22), (3.23) and (3.13) into the continuity equation (3.24) gives a linear system of Poisson-type equation at all grid cells in the form of equation (3.21). The non-hydrostatic solution of the surface elevation is calculated by equation (3.24).

Cartesian coordinate system model was applied to the case for the Seto inland sea because of narrow area for tsunami propagation but complicate coastal geometry. Fault model used is Aida model for 1854 Ansei Nankai earthquake Mw 8.4, calibrated using observed data as shown in Table 3.2.(Manshinha & Smylie, 1971). Fig.3.9 shows past Nankai eqrthquake epicenter locations. Four nested grids were used and Fig.3.10 shows the maximum tsunami height in the Area 2 with 450m grid size (Yamanaka et al, 2008). Fig.3.11 is tsunami prevailing time in the Area 2. Most area in Seto inland sea show that tsunami waves stay for 10hours, except some locations. Tsunami waves propagate through narrow channels which located

eastern and western end of the sea and wave characteristics were changed by complex topography. From simulation result, tsunami height in the Seto inland sea was less than 1m, except Osaka bay and Harima-nada sea areas. Wave period of 50 min was propagated from western strait and passed through the Seto inland sea. At some time later, wave period of 50 min also propagated eastern strait, encountered the wave from western and passed through the Seto inland sea.

However, latest researches pointed out that maximum tsunami height in Seto inland sea would appear more than 10 hours after tsunami occurrence by multiple reflected waves caused by topographical feature, enclosed and complex shoreline. This means that multiple amplification of tsunami wave and local drastic fluctuation might occur in inland sea area.

Table 3.2 Subfault parameters (after Aida, 1981)

Fault No.	Lat(°N)	Long(°E)	d(km)	$\theta(°)$	$\delta(°)$	$\lambda(°)$	L(km)	W(km)	U(km)
①	32.7	134.7	1	250	20	117	150	120	630
②	33.41	136.2	10	250	10	127	150	70	470
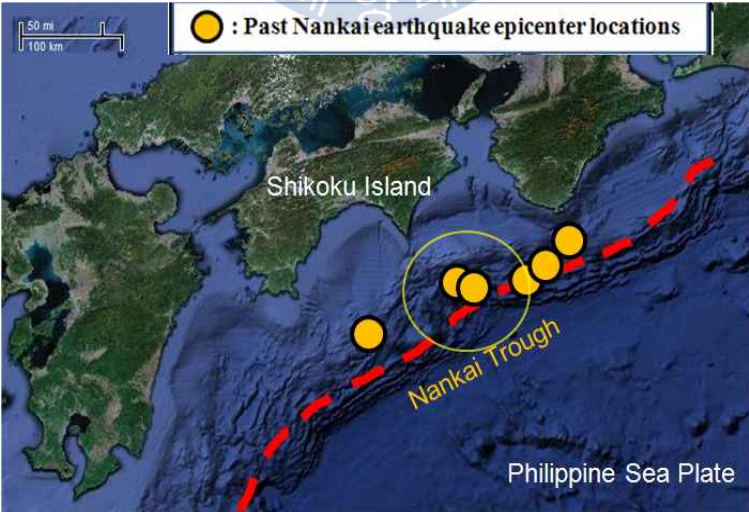
Fig.3.9 Location of epicenter Nankai earthquakes
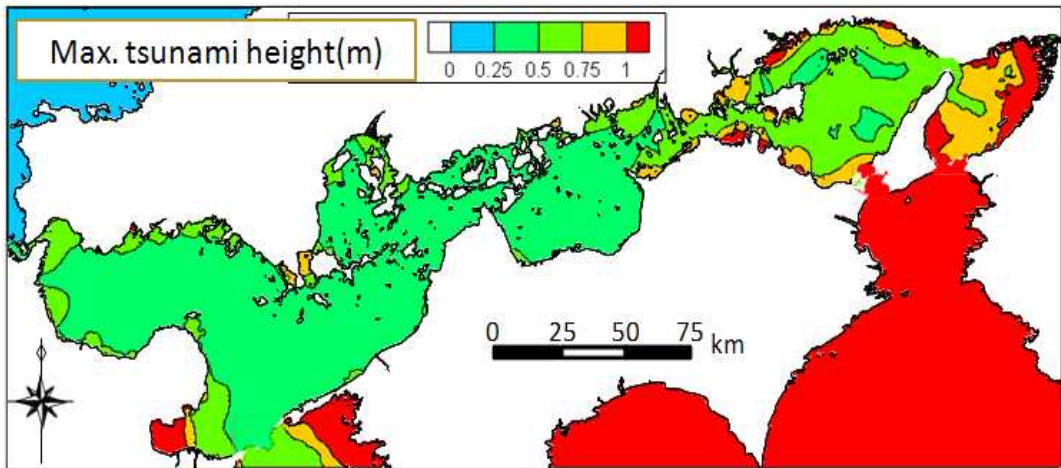
Fig.3.10 Maximum tsunami response in the Seto inland sea
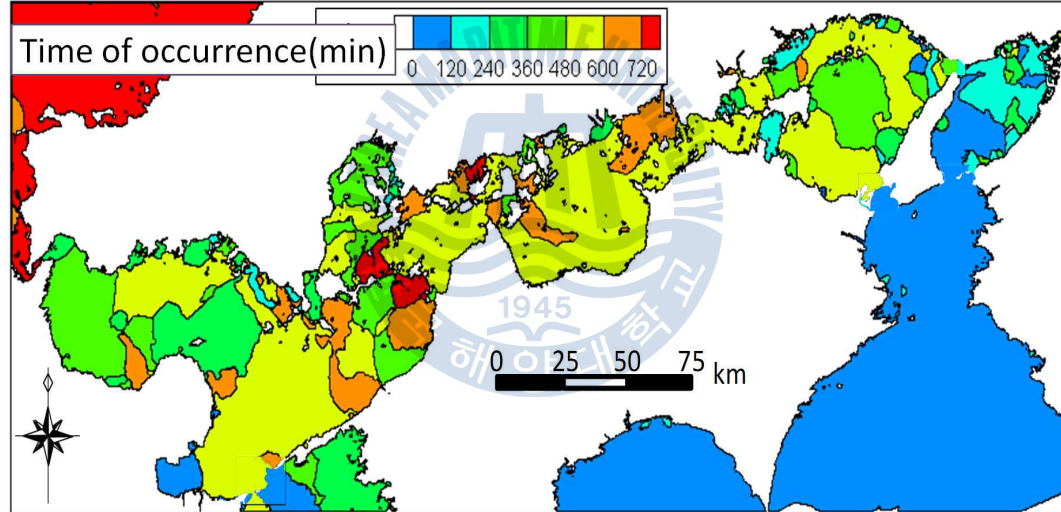
Fig.3.11 Tsunami prevailing time in the Seto inland sea
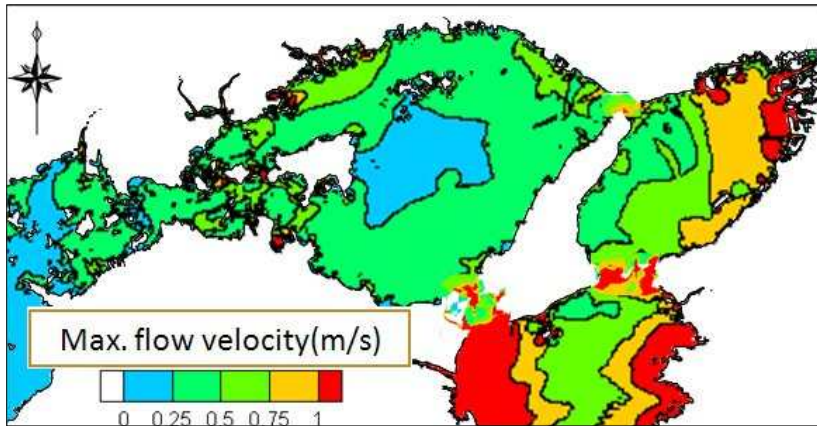
Fig.3.12 Maximum flow velocity in the Seto inland sea
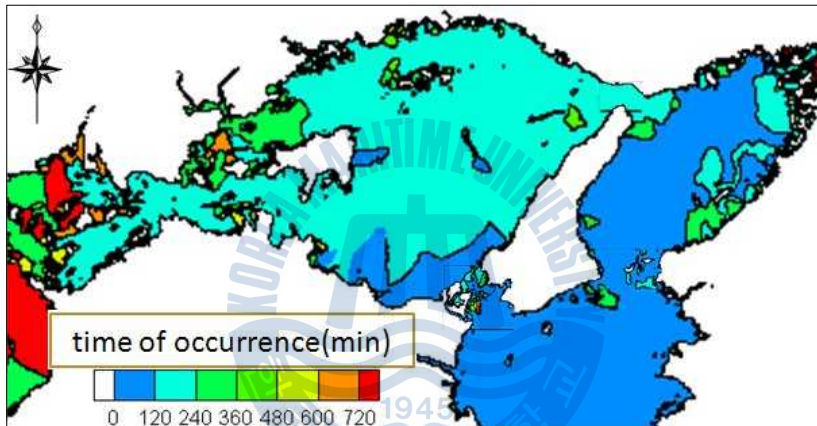
Fig.3.13 Time of occurrence of max. flow in the Seto inland sea
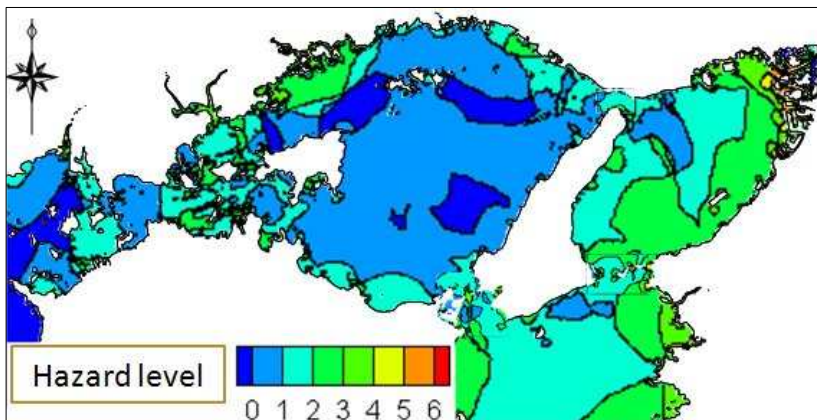
Fig.3.14 Hazard level in the Seto inland sea

Chapter 4 Resonance Analysis

Spectral analysis of the computed surface elevation and investigation of the complex amplitude over the grid level 2 give understanding of the surface motion along the Korean coast and in the Seto inland sea as a function of oscillation period.

4.1 Open Coast Analysis

Resonance amplification of the 1983 Akita tsunami occurs at a number of periods associated with standing waves over the coastal slope and embayment along the Korean coast. Fig.4.1 shows spectral energy and peak period of the tsunami in Korean coastal waters predicted by the numerical model. Following the method of Munger and Cheung (2008), a fast Fourier transform of the computed surface elevation provides the amplitude and phase as functions of frequency, together with the peak period corresponding to maximum amplitude and energy. Strong amplifications at Ulchin, Youngil Bay, Ulsan of South Korea, and Younghung and Hamhung Bay of North Korea are represented and the corresponding peak periods are shown in Fig.9, too. The most prominent energy concentration is over Youngil Bay of South Korea and Hamhung Bay of North Korea, where a combination of the harmonic modes of oscillation occurs. Coastal regions with high energy are located in large embayment, where the tsunami triggers the fundamental mode of oscillation.

Those well studied location of basin oscillation are Kahului and Hilo Bay, Hawaii (Munger & Cheung, 2008), Arauco Gulf, Chile (Yanazaki & Cheung,

2011), and Pago Pago Harbor and Fagaitua Bay, American Samoa (Roeber et al., 2010). Rabinovich & Monserrat (1998) made a comparative analysis of tsunami oscillations in different bays. Fig.4.2 and Fig.4.3 show the amplitude and phase of eight dominant oscillation modes between 12 to 86 min period associated with standing waves over the peninsula slope and shelf complex as well as the embayment along the east coast of Korea. The 200m depth contour shows the outline of the peninsula shelf. The phase plots in Fig.4.3 show some of the oscillation modes contain partial standing waves. However, the nodes were not defined well, because of shelf and coast configurations.
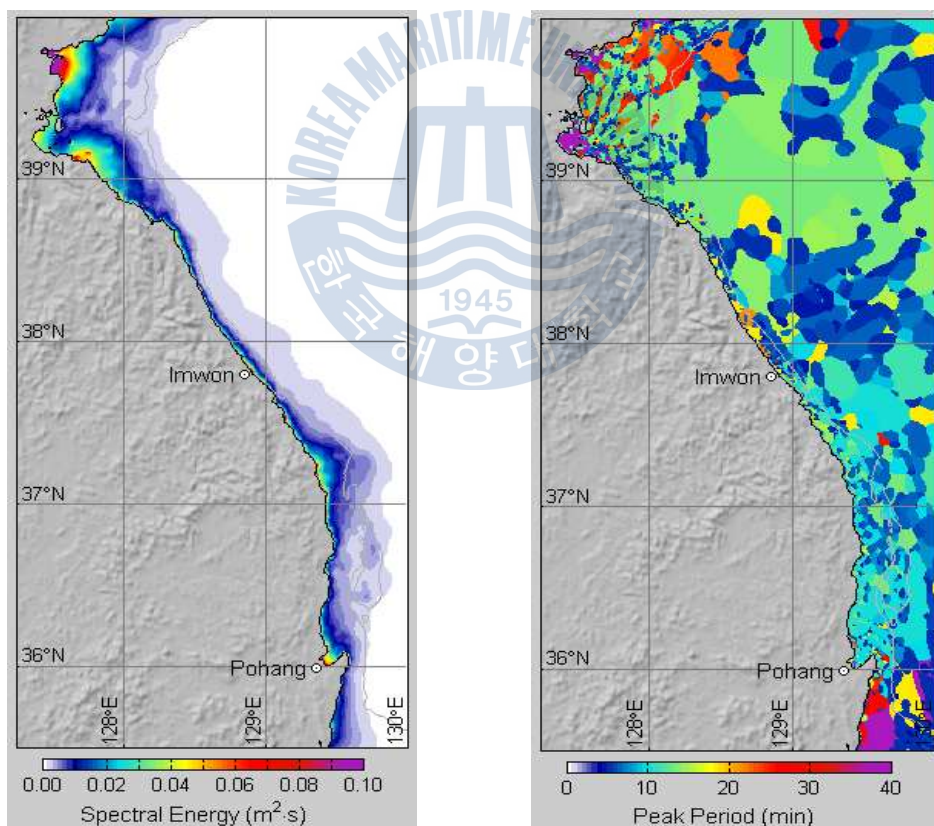
Fig.4.1 Spectral energy and peak period in the east coast of Korea
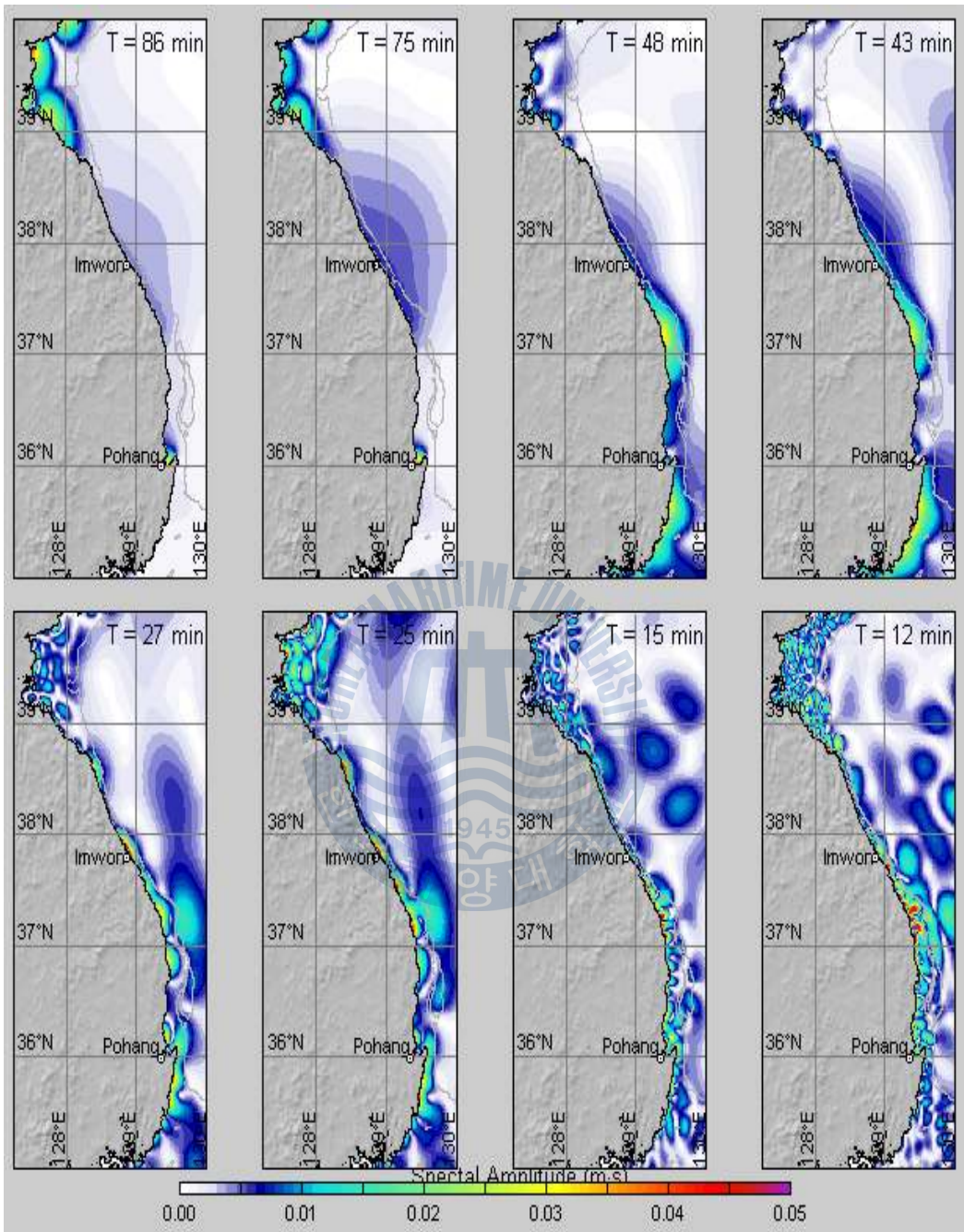
Fig.4.2 Amplitude of resonance modes along the east coast of Korea
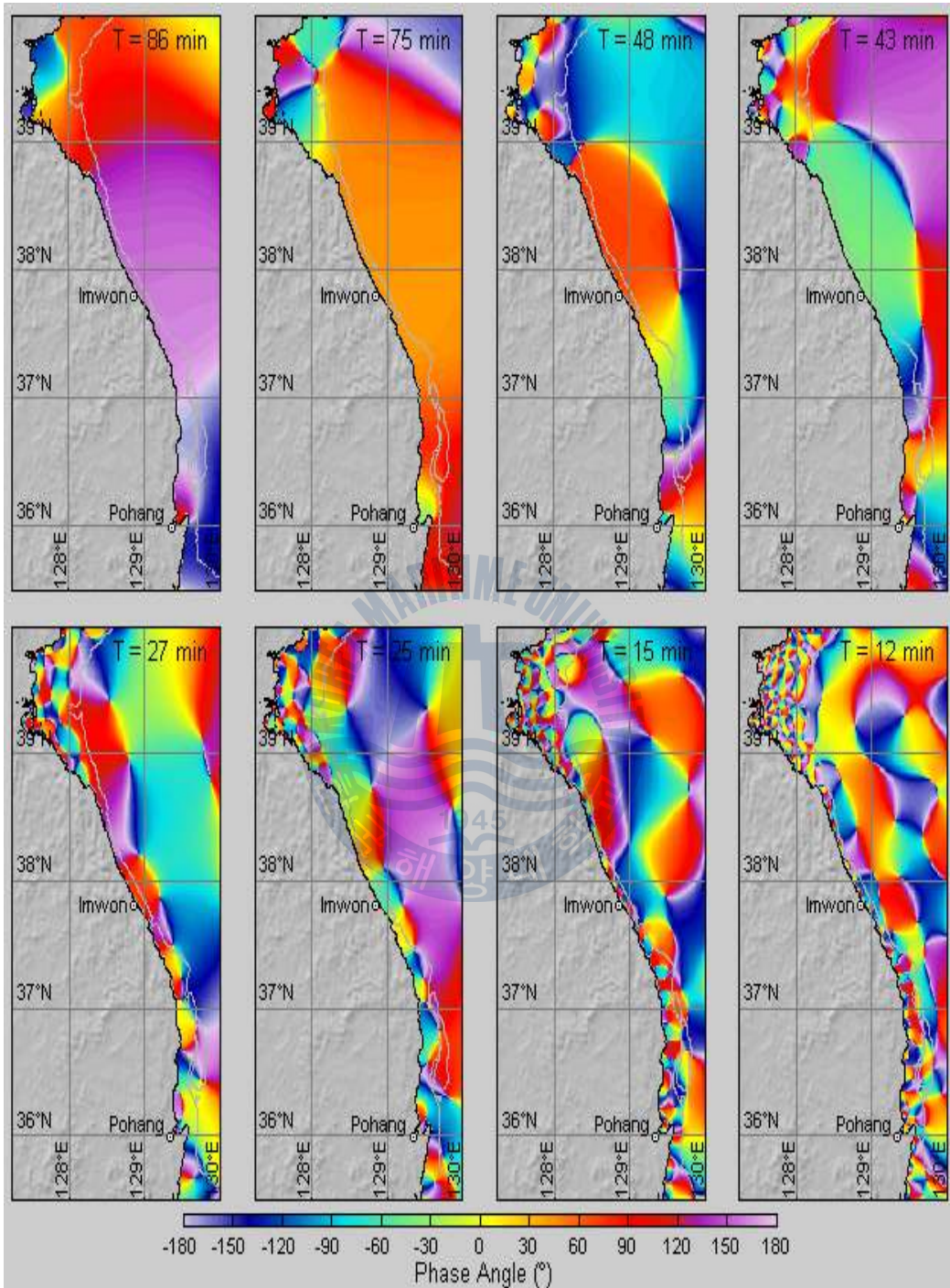
Fig.4.3 Phase angle of resonance modes along the east coast of Korea

The 86min amplitude plot shows a system of standing waves, which is a coastal trapped oscillation at Younghung and Hamhung Bay of North Korea. This oscillation is prolonged to 75min, which is a dominant mode at Youngil Bay of South Korea. The shelf width and shoreline configuration dominate the resonant amplification with periods between 12 and 27min. These coastal trapped waves are the primary source of oscillations in bays, narrow shelves, and harbors observed during the tsunami.

4.2 Inland Sea Analysis

1) Wavelet Analysis

After the passage of tsunami wave, fluctuation of sea level continued at some points. Maximum tsunami height in the Seto inland sea appeared more than 10 hours after the time of tsunami occurrence. In order to analyze the resonance response in the inland sea, nine points at Harima-nada in Seto inland sea were selected as shown in Fig.4.4.

Fig.4.4 Evaluation points in Harimanada

Fig.4.5 through Fig.4.8 show the time series of sea level variation at these locations. The transform of a signal is another form of representing the signal without changing the information content in it. The wavelet transform can be used to analyze time series that contain nonstationary power at many different frequencies. The wavelet transform provides a temporal-frequency analysis of the tsunami wave. Assume that one has a time series, x_n, with equal time spacing δt and $n = 0 \cdots N-1$. Also assume that one has a wavelet function, $\Psi_0(\eta)$, that depends on a nondimensional time parameter η. To be admissible as a wavelet, this function must have zero mean and be localized in both time and frequency space (Farge 1992).

The signal to be analyzed is multiplied with a mother wavelet function just as it is multiplied with a window function. The term wavelet function is used generically to refer to either orthogonal or nonorthogonal wavelets. Among a number of wavelet functions, Morlet function which is symmetric in shape as shown in Fig. 4.9 (Merry, 2005), was chosen for this study. An example is the Morlet wavelet, consisting of a plane wave modulated by a Gaussian:

$$\Psi_0(\eta) = \pi^{-1/4} e^{i\omega_0 \eta} e^{-\eta^2/2} \tag{4.1}$$

where ω_0 is the nondimensional frequency and is taken to be a value to satisfy the admissibility condition. Detail description on wavelet transform model formulation with this function was referred to Torrence & Compo (1998).

In general, the wavelet transform, at high frequencies, gives good time resolution and poor frequency resolution, while at low frequencies, the Wavelet Transform gives good frequency resolution and poor time resolution.
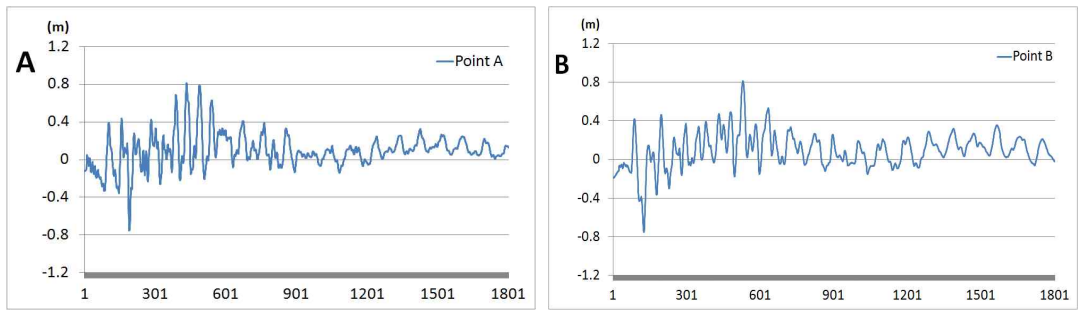
Fig.4.5 Time series of tsunami waves at points A and B
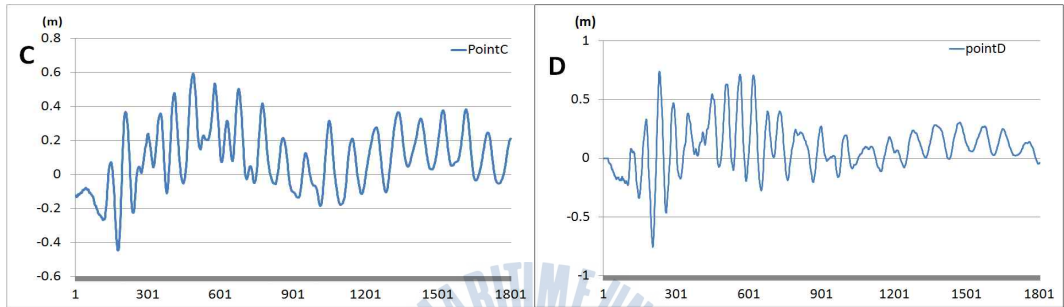
Fig.4.6 Time series of tsunami waves at points C and D
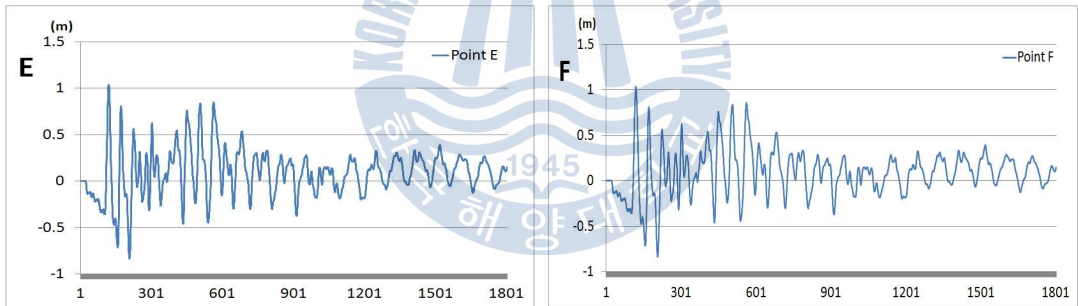
Fig.4.7 Time series of tsunami waves E and F
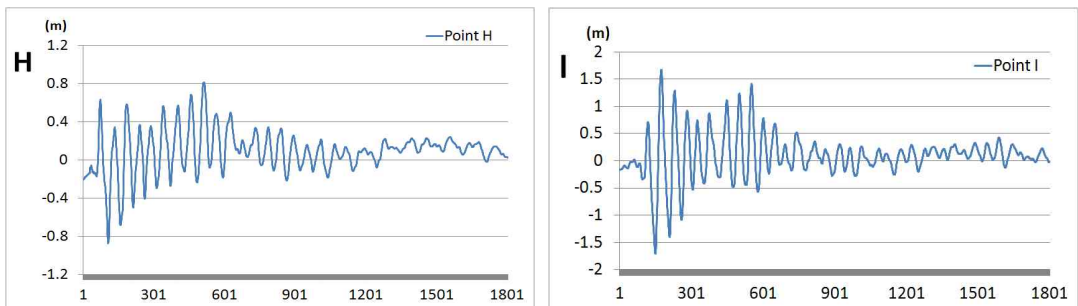
Fig.4.8 Time series of tsunami waves at points H and I
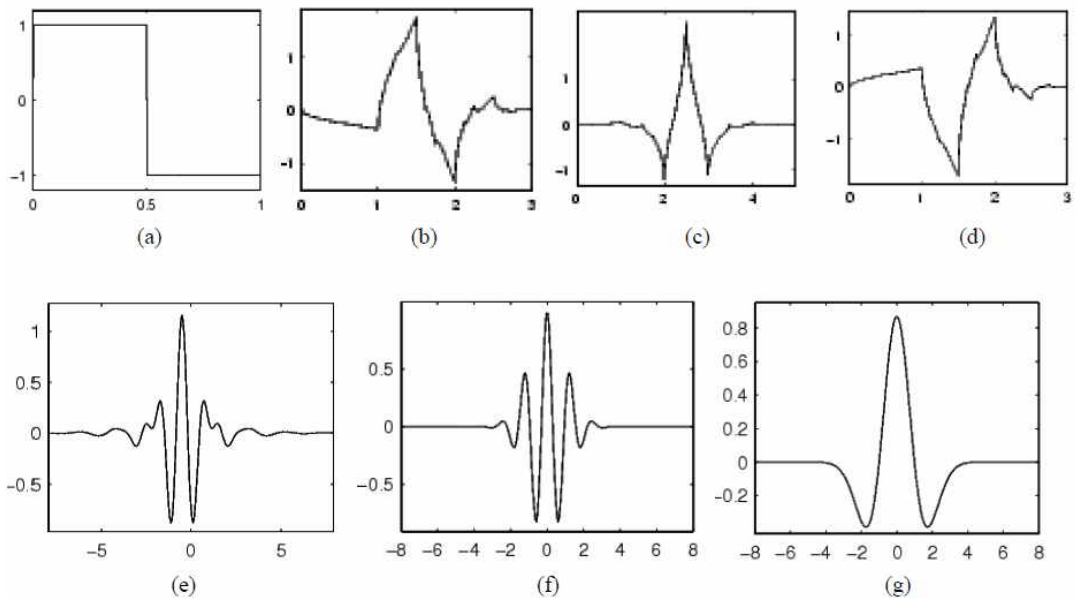
Figure 4.9 Wavelet functions (a) Haar (b) Daubechies4 (c) Coiflet1
(d) Symlet2 (e) Meyer (f) Morlet (g) Mexican Hat

Fig.4.10 and Fig.4.11 show the result of wavelet transform of tsunami wave responses. The x-axis is the wavelet location in time(min) and the y-axis is the wavelet period(min).

It gives a predominant wave period corresponding to the large value area by time period power spectra. The sea level was changed irregularly up to 1000min but after this, the sea level continued to oscillate with opposite phase in some points. It shows different patterns depending on the location but there exists an oscillation mode of 100min period. It is now much clearer that there is large power in the 50min and exists a oscillation mode of 100min period, which is lasting more than 1000min. From this result, it is considered that a seiche motion was induced in this inland sea.
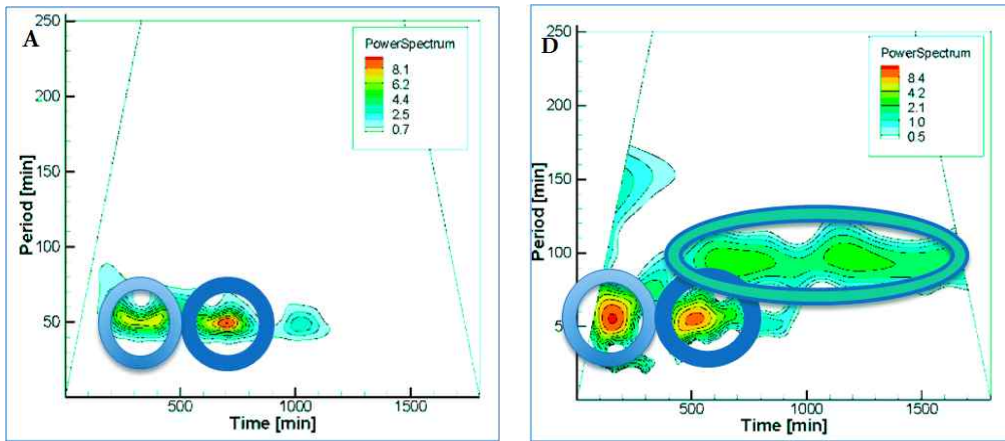
Fig.4.10 Variation of periods at points A and D
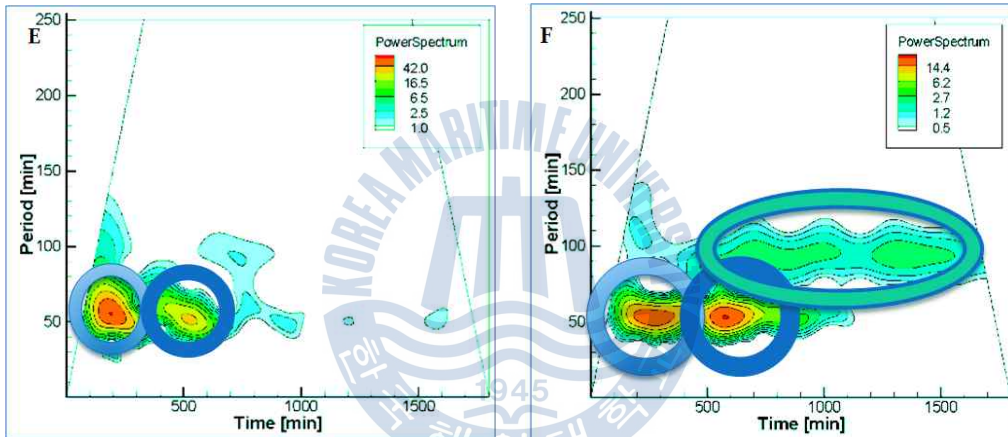
Fig.4.11 Variation of wave periods at points E and F

2) Coherence Analysis

In order to analyze the oscillation mode in the detail, we made coherence analysis for the selected stations. From the coherence analysis for time series of two different tsunami waves in terms of frequency, it is possible to analyze the similarity of wave pattern.

It was restricted the theory to second order statistics and introduce therefore the second-order correlation function $\Gamma(\mathbf{r_1}, \mathbf{r_2}; t_1, t_2)$, known as the mutual coherence function as shown in Hoenders & Bertolotti (2005),

$$\Gamma(\boldsymbol{r_1},\boldsymbol{r_2};t_1,t_2) \equiv\ <\psi(\boldsymbol{r_1},t_1)\psi^*(\boldsymbol{r_2},t_2)>$$
(4.1)

where $*$ indicates complex conjugation and the brackets $<>$ indicate that the average of the quantity $\psi(\boldsymbol{r_1},t_1)\psi^*(\boldsymbol{r_2},t_2)$ has to be taken over the appropriate space-time ensemble. The normalized mutual coherence function lies between zero and 1:

$$0 \le |\gamma(\boldsymbol{r_1},\boldsymbol{r_2};t_1,t_2)| \le 1.$$
(4.2)

The value of 1 for the coherence function means that the two points coincided with each other and 0 means no coincidence between two points.

In this study each station of Fig 4.4 was linked with the other stations to relate with and analyzed the characteristic oscillation mode. Selected group for coherence analysis are shown in Fig.4.12 through Fig.4.21. A-D shows some of coherence with in phase.

However, D-E and C-G have strong coherence but opposite position. F-D shows similar pattern. B-G is in phase but B-E is out of phase during more than 100 minutes. This result means that tsunami wave induce tsunami resonance in the inland sea both in northeast-southwest and northwest-southeast directions. This is the reason why the fluctuation of sea level was continued. Industrial area near this inland sea is being expanded and the use of sea transportation increases in spite of narrow seaway. Population near shore line and aqua-farming equipments moored are getting increased. Therefore, there is a possibility of occurrence of new type disaster to ship and aqua-farming equipment in inland sea.
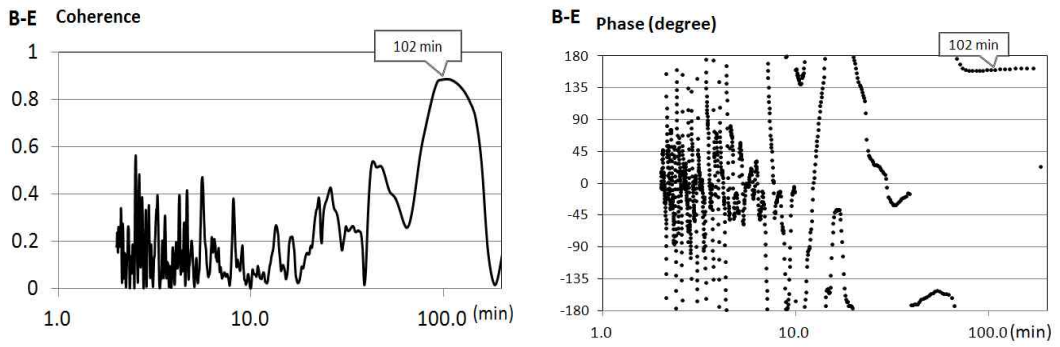
Fig.4.12 Coherence analysis for period and phase at Point B-E
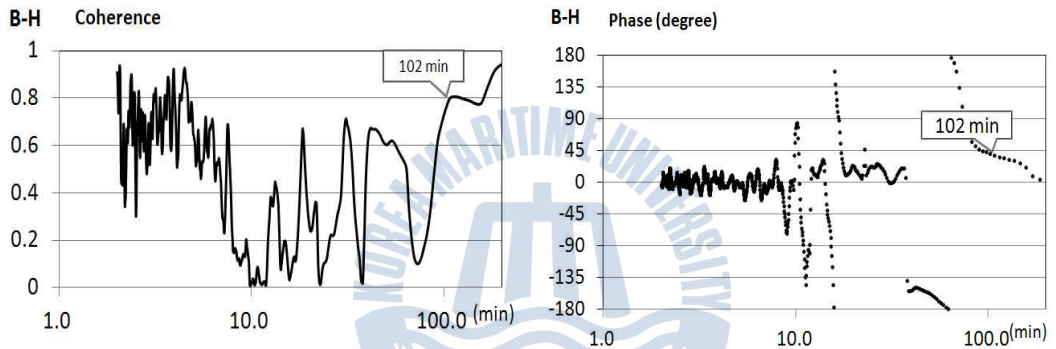
Fig.4.13 Coherence analysis for period and phase at Point B-H
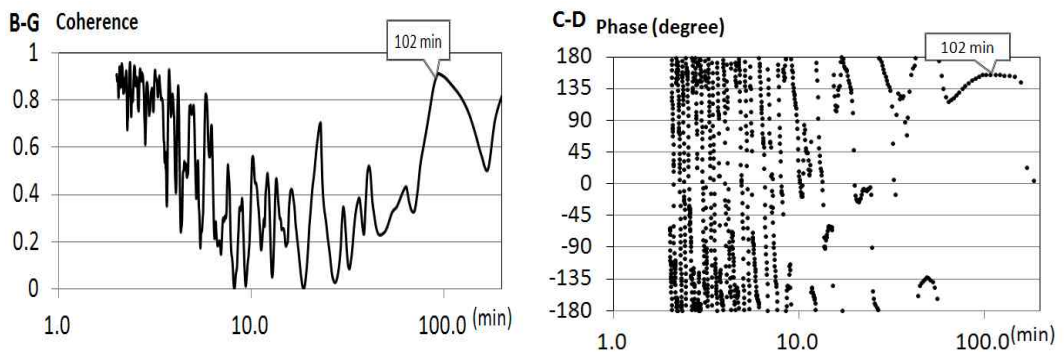
Fig.4.14 Coherence analysis for period and phase at Point B-G
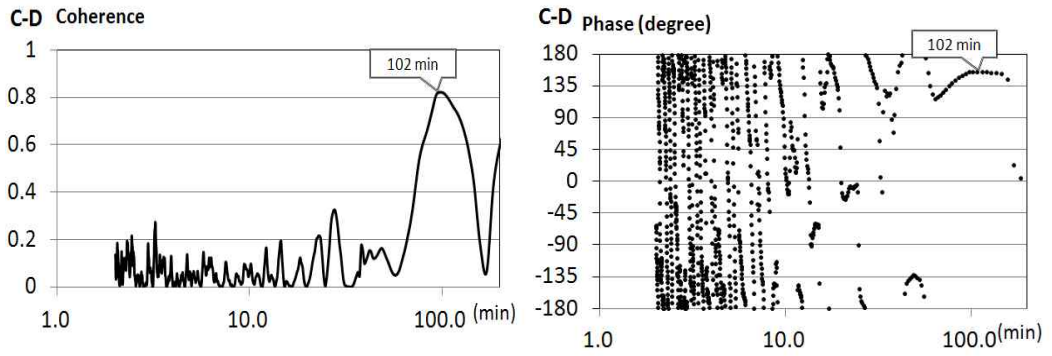
Fig.4.15 Coherence analysis for period and phase at Point C-D
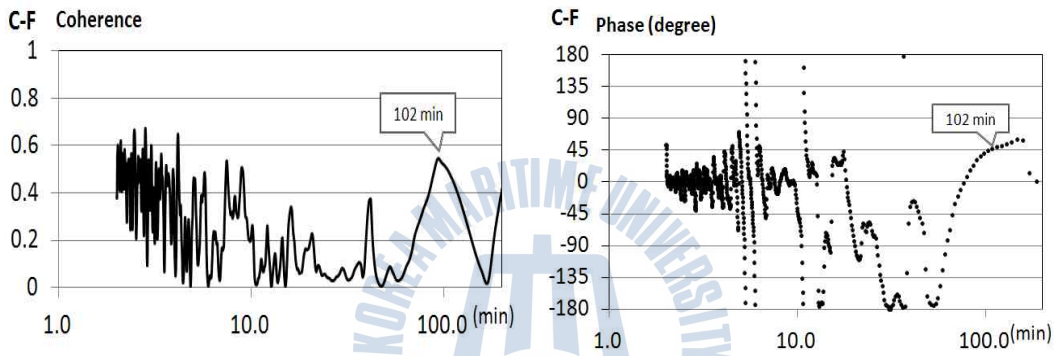
Fig.4.16 Coherence analysis for period and phase at Point C-F
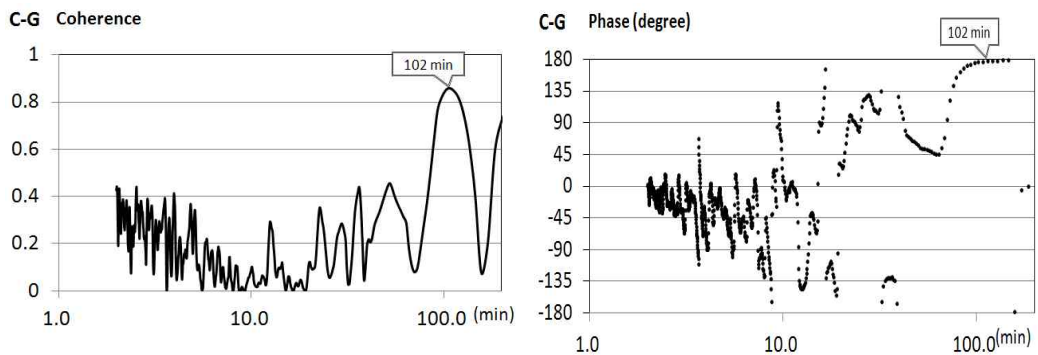
Fig.4.17 Coherence analysis for period and phase at Point C-G
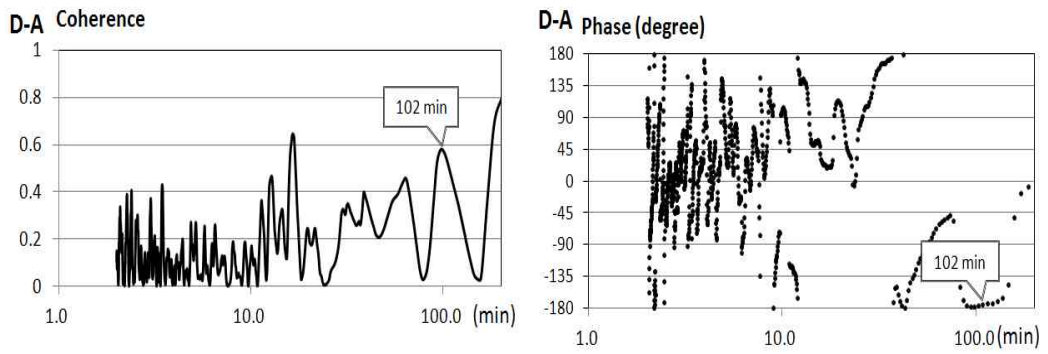
Fig.4.18 Coherence analysis for period and phase at Point D-A
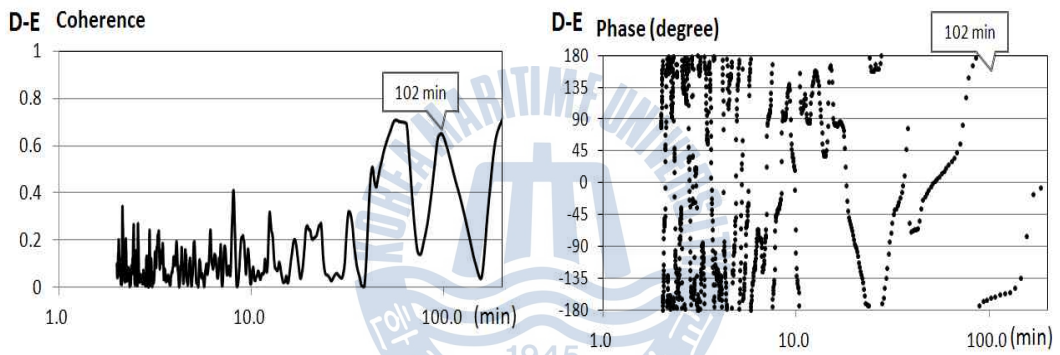
Fig.4.19 Coherence analysis for period and phase at Point D-E
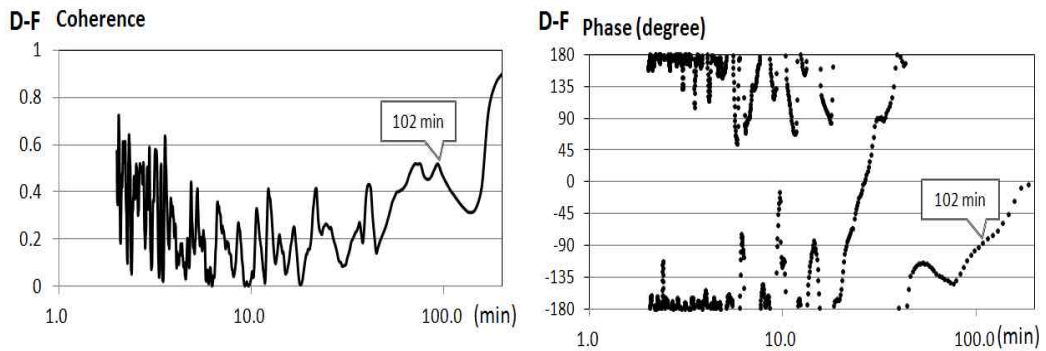
Fig.4.20 Coherence analysis for period and phase at Point D-F
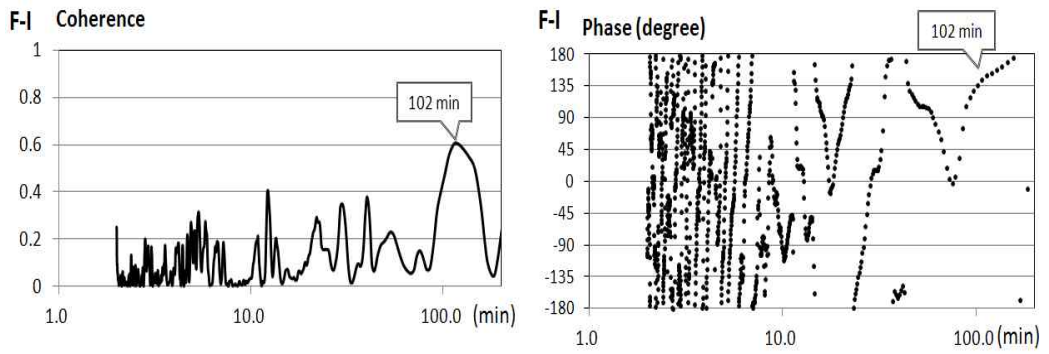
Fig.4.21   Coherence analysis for period and phase at Point F-I

Chapter 5 Result and Discussions

The recent trend for earthquakes and tsunamis shows stronger and higher runup. For prediction of tsunami waves at the coastal cities, it is necessary to reform static and dynamic earthquake parameters. Present study with the grid-nesting scheme can model entire tsunami evolution from its generation, propagation, transformation, and runup. Basic analysis for the previous tsunami events in Korea-Japan sea and Seto inland sea areas for the inputs of numerical model analysis. Both the spherical coordinate system model and cartesian coordinate system model were formulated and applied to these seas, and resonance analysis was made together with wave runup and flow speed. For more specific analysis of tsunami resonance, wavelet and coherence analyses were introduced. Followings are the summary of the analyses:

1) From the numerical analysis more accurate and high-resolution water level variations and runups over fringing reef during the Central East Korea-Japan Sea Earthquake Tsunami were provided. Macro scale of tsunami wave resonance patterns in the east coast of Korean peninsula were analyzed with the two nested grid system. Wonsan(Younghung, Hamhung) Bay in North Korea 86 min period caused the first mode(longest period) and this also happened in Youngil-Bay in south Korea. Other modes of resonance were investigated in terms of energy spectrum and amplitude and phase resonance mode.

It might need more investigation with narrow domain with dense grid nesting together with field records, which would be completed at the next study. Other nested sites for industry plants are necessary to be analyzed

in terms of spectra, runup, and resonance, too. However, the simulations presented for Korean coast suggest that bathymetric interaction with the surrounded coastal boundaries is responsible for the tsunami resonance.

2) From the result of the inland sea tsunami analysis for 1854 Ansei Nankai earthquake, tsunami waves propagate through narrow channels which located at the eastern and western end of the sea and wave characteristics were changed by complex topography. According to wavelet analysis for the inland sea, long-term fluctuations over 100min were generated by tsunami resonance and this might cause problems on mooring ships and navigation inland sea areas.

The simulations presented for Seto inland sea area suggest that narrow entrance and shallow basin surrounded by islands and coastal boundaries are responsible for the generation of tsunami resonance and late arrivals of its formulation. At 102min period, strong modes, giving a coherence coefficient greater than 0.8, observed both in northeast-southwest and northwest-southeast directions at the Seto inland sea.
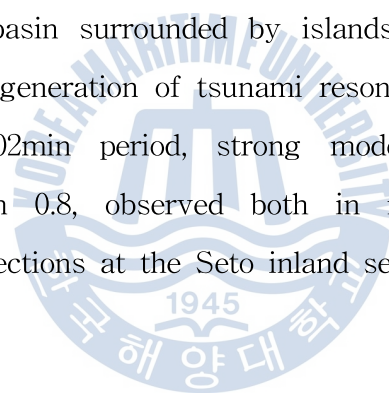
References

Aida, I. (1984), A Source Model of the Tsunami Accompanying the 1983 Nihonkai-Chubu Earthquake, *Bull. Eqrthq. Res.I nst. Univ. Tokyo*, 59, pp.93-104.

Cheung, K.F. and Yamazaki, Y. (2010), NEOWAVE user manual, University of Hawaii at Manoa.

Farge, M. (1992), Wavelet transforms and their applications to turbulence, *Annu. Rev. Fluid Mech.,* 24, pp.395‐57.

Hoenders, B.J. and Bertolotti, M. (2005), Coherece theory of electromagnetic wave propagation through stratified N-layer media, J. Opt. Soc. Am. A, 22(6), pp.1143-1150.

Kim, K.H., Ryoo, Y.G., Yu, C.H., Kang, S.Y., and Kim, H.J. (2011), Relocation of Youngduk Offshore Micro-earthquakes, Jigu-Mulli-wa-Mulli-Tamsa (Korean), 14(4), pp. 267-273.

Kowalik, Z. and Murty, T.S. (1993). Numerical Modeling of Ocean Dynamics. World Scientific, Singapore, 481p.

Mader, C.L. (1988), *Numerical Modeling of Water Waves,* University of California Press, California, 206p.

Mansinha, L. and Smylie, E. (1971), The Displacement Field of Inclined Faults, *Bull. Seismol. Soc. Am. 61*, pp.1433-1440.

Merry, R.J.E. (2005), Wavelet Theory and Applications-A literature study, Eindhoven University of Technology, Eindhoven, 49p.

MKE (2010), Nuclear Power, Our Hope for Low Carbon and Green Growth, *25th Korea Atomic Industrial Forum.*

Munger, S. and Cheung, K.F. (2008), Resonance in Hawaii waters from the 2006 Kuril Islands Tsunami, *Geophysical Research Letters*, 35, L07605, pp.1-7.

Okada, Y. (1985), Surface deformation due to shear and tensile faults in a half space. Bulletin of the Seismological Society of America, 75(4),

pp.1135-1154.

Peregrine, D.H. (1967), Long waves on a beach. Journal of Fluid Mechanics, 27(4), pp.815-827.

Rabinovich, A.B. and Monserrat, S. (1998), Generation of Meteorological Tsunamis (Large Amplitude Seiches) near the Balearic and Kuril Islands, *Natural Hazards*, **18**(1), pp.27-55.

Roeber, V., Yamazaki, Y., and Cheung, K.F. (2010), Resonance and impact of the 2009 Samoa Tsunami around Tutuila, American Samoa, *Geophysical Research Letters*, **37**, L21604, pp.1-8.

Titov, V.V. and Synolakis, C.E. (1998), Numerical modeling of tidal wave runup. *Journal of Waterway, Port, Coastal, and Ocean Engineering*, 124(4), pp.157-171.

Torrence, C. and Compo, G. P. (1998), A Practical Guide to Wavelet Analysis, *Bull. Amer. Meteor. Soc.*, 79, pp.61-78.

Ward, S. N.(2000),"Tsunamis" in *The Encyclopedia of Physical Science and Technology*, ed. R. A. Meyers, Academic Press.

Yamanaka, R., Kozuki, Y., Tanabe, S., Iwaka, K., and Murakami, H. (2008), Spatiotemporal analysis of Tsunami wave property and hazardous sea area in Seto Island Sea, Tokushima University.

Yamazaki, Y., Wei, Y., Cheung, K.F., and Curtis, G.D. (2006), Forecast of tsunamis generated at the Japan-Kuril-Kamchatka source region. *Natural Hazards*, 38(3), pp.411-435.

Yamazaki, Y. (2010), Depth-integrated, Non-hydrostatic Model with Grid Nesting for Tsunami Generation, Propagation, and Runup, PhD Dissertation, Ocean Resources Engineering, University of Hawaii at Manoa.

Yamazaki, Y. and Cheung, K.F. (2011), Shelf resonance and Impact of near-field tsunami generated by the 2010 Chile earthquake, *Geophysical Research Letters*, **38**, L12605, pp.1-8.